

# Detailed Report of the MuLan Measurement of the Positive Muon Lifetime and Determination of the Fermi Constant

V. Tishchenko,<sup>1</sup> S. Battu,<sup>1</sup> R.M. Carey,<sup>2</sup> D.B. Chitwood,<sup>3</sup> J. Crnkovic,<sup>3</sup> P.T. Debevec,<sup>3</sup>  
S. Dhamija,<sup>1</sup> W. Earle,<sup>2</sup> A. Gafarov,<sup>2</sup> K. Giovanetti,<sup>4</sup> T.P. Gorringer,<sup>1</sup> F.E. Gray,<sup>5</sup> Z. Hartwig,<sup>2</sup>  
D.W. Hertzog,<sup>3,6</sup> B. Johnson,<sup>7</sup> P. Kammel,<sup>3,6</sup> B. Kiburg,<sup>3</sup> S. Kizilgul,<sup>3</sup> J. Kunkle,<sup>3</sup> B. Lauss,<sup>8</sup>  
I. Logashenko,<sup>2</sup> K.R. Lynch,<sup>2,9</sup> R. McNabb,<sup>3</sup> J.P. Miller,<sup>2</sup> F. Mulhauser,<sup>3,8</sup> C.J.G. Onderwater,<sup>3,10</sup>  
Q. Peng,<sup>2</sup> J. Phillips,<sup>2</sup> S. Rath,<sup>1</sup> B.L. Roberts,<sup>2</sup> D.M. Webber,<sup>3</sup> P. Winter,<sup>3</sup> and B. Wolfe<sup>3</sup>

(MuLan Collaboration)

<sup>1</sup>*Department of Physics and Astronomy, University of Kentucky, Lexington, KY 40506, USA*

<sup>2</sup>*Department of Physics, Boston University, Boston, MA 02215, USA*

<sup>3</sup>*Department of Physics, University of Illinois at Urbana-Champaign, Urbana, IL 61801, USA*

<sup>4</sup>*Department of Physics, James Madison University, Harrisonburg, VA 22807, USA*

<sup>5</sup>*Department of Physics and Computational Science, Regis University, Denver, CO 80221, USA*

<sup>6</sup>*Department of Physics, University of Washington, Seattle, WA 98195, USA*

<sup>7</sup>*Department of Mathematics and Physics, Kentucky Wesleyan College, Owensboro, KY 42301, USA*

<sup>8</sup>*Paul Scherrer Institute, CH-5232 Villigen PSI, Switzerland*

<sup>9</sup>*Department of Earth and Physical Sciences, York College, City University of New York, Jamaica, NY 11451, USA*

<sup>10</sup>*KVI, University of Groningen, NL-9747AA Groningen, The Netherlands*

(Dated: November 27, 2024)

We present a detailed report of the method, setup, analysis and results of a precision measurement of the positive muon lifetime. The experiment was conducted at the Paul Scherrer Institute using a time-structured, nearly 100%-polarized, surface muon beam and a segmented, fast-timing, plastic scintillator array. The measurement employed two target arrangements; a magnetized ferromagnetic target with a  $\sim 4$  kG internal magnetic field and a crystal quartz target in a 130 G external magnetic field. Approximately  $1.6 \times 10^{12}$  positrons were accumulated and together the data yield a muon lifetime of  $\tau_\mu(\text{MuLan}) = 2196980.3(2.2)$  ps (1.0 ppm), thirty times more precise than previous generations of lifetime experiments. The lifetime measurement yields the most accurate value of the Fermi constant  $G_F(\text{MuLan}) = 1.1663787(6) \times 10^{-5}$  GeV<sup>-2</sup> (0.5 ppm). It also enables new precision studies of weak interactions via lifetime measurements of muonic atoms.

PACS numbers: 06.20.Jr, 12.15.Ji, 13.35.Bv, 14.60.Ef

## I. INTRODUCTION

Weak interactions are germane to topics from big-bang nucleosynthesis and stellar hydrogen burning, to archaeological dating and medical imaging, as well as fundamental nuclear and particle physics. Unlike electromagnetic and strong interactions, all particles participate in weak interactions, and every process appears consistent with a universal strength for the weak force. This strength is governed by the Fermi constant [1].

The value of the Fermi constant  $G_F$  is best determined by the measurement of the muon lifetime  $\tau_\mu$  for two reasons; the muon lifetime is well suited to precision time measurements and the pure-leptonic character of muon decay permits an unambiguous theoretical interpretation. Until recently, the uncertainty in  $G_F$  was 17 parts-per-million (ppm); it originated from a 9 ppm contribution from the existing measurements of the muon lifetime and a 15 ppm contribution from the knowledge of the theoretical relation between the muon lifetime and the Fermi constant.

The theoretical uncertainty arose from a limited knowledge of the 2-loop QED corrections to the muon decay rate. In 1999, van Ritbergen and Stuart (vRS) evaluated these corrections, thus establishing the relation between

$G_F$  and  $\tau_\mu$  to sub-ppm level [2–4]. Their work was the motivation for our part-per-million measurement of the positive muon lifetime.

### A. Relation between $G_F$ and the muon lifetime

The V-A current-current Fermi interaction is a convenient effective theory for the description of the charged-current weak interaction and the definition of the Fermi constant. Although non-renormalizable, it is well suited to the low-energy limit of the electroweak interaction and neatly separates the parameterization of the weak interaction from corrections due to electromagnetic interactions. In particular,  $G_F$  encapsulates all the weak interaction effects in the low-energy effective theory [2].

Feynman diagrams for ordinary decay at tree- and 1-loop level in Fermi theory are shown in Fig. 1. At the part-per-million level all appreciable corrections to the tree-level diagram arise from QED radiative corrections. Most importantly the hadronic effects are virtually nonexistent, their leading terms arising as 2-loop QED corrections that contribute only 0.2 ppm to  $\tau_\mu$  [4].

Despite such simplifications the extraction of  $G_F$  from  $\tau_\mu$  to sub-ppm level requires an exhaustive calculation of

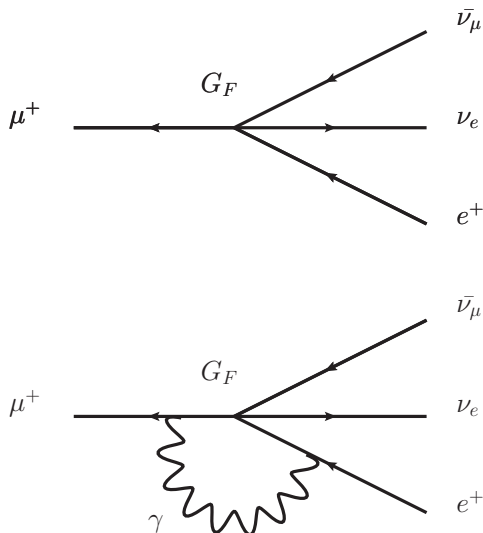


FIG. 1: Feynman diagrams for ordinary muon decay in Fermi theory. The upper graph shows the tree-level diagram for the ordinary decay amplitude while the lower graph shows the 1-loop QED correction to the ordinary decay amplitude.

first- and second-order QED radiative corrections. In vRS, the authors expressed the relation between the Fermi constant and the muon lifetime as a perturbative expansion

$$\frac{1}{\tau_\mu} = \frac{G_F^2 m_\mu^5}{192\pi^3} \left( 1 + \sum_i \Delta q^{(i)} \right) \quad (1)$$

where  $m_\mu$  is the muon mass and  $\sum \Delta q^{(i)}$  describes the phase space ( $\Delta q^{(0)}$ ), first-order QED ( $\Delta q^{(1)}$ ), second-order QED ( $\Delta q^{(2)}$ ), *etc.*, theoretical corrections.

With an uncertainty arising from the theoretical corrections of 0.14 ppm [2–5]<sup>1</sup> and an uncertainty arising from the muon mass of 0.08 ppm [6], the overwhelming uncertainty in the Fermi constant became the experimental determination of the muon lifetime.

## B. Relation between $G_F$ and the Standard Model

Once  $G_F$  is determined from  $\tau_\mu$  using Eqn. 1, it can be related to the fundamental parameters of any high energy

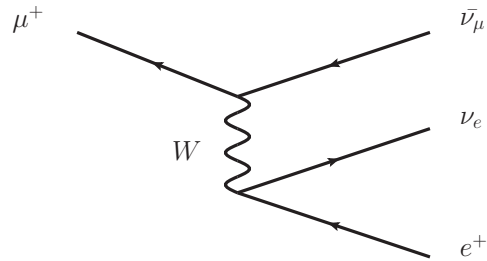


FIG. 2: Standard model tree-level diagram of ordinary muon decay showing the W-boson mediating the electroweak interaction between the weak leptonic currents.

theory, *e.g.* the electroweak interaction in the Standard Model. The relation between the Fermi constant and the Standard Model can be written as a perturbative expansion of the electroweak interaction

$$\frac{G_F}{\sqrt{2}} = \frac{g^2}{8M_W^2} \left( 1 + \sum_i r_i \right) \quad (2)$$

where  $1/M_W^2$  represents the low-energy limit of the tree-level propagator corresponding to  $W$ -boson exchange (See Fig. 2) and  $\sum r_i$  incorporates all higher-order electroweak interaction corrections [7]. Note that Eqn. 2 can be recast in a form with only observable quantities and the higher-order corrections

$$M_W^2 \left( 1 - \frac{M_W^2}{M_Z^2} \right) = \frac{\pi\alpha}{\sqrt{2}G_F} \left( 1 + \sum_i r_i \right). \quad (3)$$

This relation between the Fermi constant  $G_F$ , fine structure constant  $\alpha$ , and weak boson masses  $M_W$  and  $M_Z$ , is an important prediction of the Standard Model.

## C. Summary of previous measurements

In 1999, at the time of the vRS publications, the PDG world average of the muon lifetime was  $\tau_\mu = 2.19703 \pm 0.00004 \mu\text{s}$  [8]. This average was largely determined by three measurements: Giovanetti *et al.* [9], Bardin *et al.* [10] and Balandin *et al.* [11], all conducted more than twenty five years ago. The experiments all observed the decay positrons from stopped muons in various targets.

The experiments of Giovanetti *et al.* and Balandin *et al.* both used a continuous beam. To avoid any misidentification of parent muons with detected positrons, the beams were restricted to low rates, thereby limiting the accumulated statistics of decay positrons.

The Bardin *et al.* experiment used a pulsed beam with the associated time structure of the Saclay electron linac. In principle, a pulsed beam technique can overcome the aforementioned rate limitations by first accumulating multiple muon stops during the beam-on period

<sup>1</sup> The original derivation of vRS was conducted in the massless electron limit. The authors assessed a theoretical uncertainty of 0.3 ppm in  $G_F$  arising from estimated mass terms at 2-loop order and neglected Feynman diagrams at 3-loop order. In 2008, Pak and Czarnecki [5] extended the work of vRS to include the 2-loop order, electron mass terms. Their work reduced the theoretical uncertainty in  $G_F$  to 0.14 ppm.

and then detecting multiple decay positrons during the beam-off period. In practice, the duty cycle at Saclay was not ideal and therefore limited the accumulated statistics of decay positrons.

Following the vRS publications, two new measurements of the muon lifetime were initiated at the Paul Scherrer Institute. The FAST experiment [12] used a finely-segmented active target to identify decay positrons with parent muons and thereby operate at somewhat higher continuous beam rates. Herein we describe the MuLan experiment [13], which made a part-per-million measurement of the positive muon lifetime using a customized time-structured muon beam. Letters describing our 2004 commissioning measurement and 2006-2007 production measurements were published in Refs. [14, 15].

## II. RELEVANT FEATURES OF DECAYS AND INTERACTIONS OF MUONS

### A. Muon decay.

The known decay modes of positive muons are ordinary muon decay  $\mu^+ \rightarrow e^+ \nu_e \bar{\nu}_\mu$ , radiative muon decay  $\mu^+ \rightarrow e^+ \nu_e \bar{\nu}_\mu \gamma$  ( $BR = 1.4 \pm 0.4 \times 10^{-2}$ ), and the rare decay  $\mu^+ \rightarrow e^+ e^+ e^- \nu_e \bar{\nu}_\mu$  ( $BR = 3.4 \pm 0.4 \times 10^{-5}$ ). In this experiment the neutrinos from muon decay were completely undetectable, the photons from radiative decay were barely detectable, and the detected positrons were overwhelmingly from ordinary decay. Although the setup did not measure the energy of the positrons, it did identify their direction.

Due to parity violation in the weak interaction, the positrons emitted in ordinary decay are distributed asymmetrically relative to the muon spin axis. The distribution is given by [1]

$$N(\theta, E) \propto 1 + A(E) \cos \theta, \quad (4)$$

where  $\theta$  is the angle between the muon spin direction and the positron momentum direction and  $A(E)$  is the energy-dependent positron asymmetry. As shown in Fig. 3, the asymmetry  $A(E)$  varies with positron energy  $E$  according to

$$A(E) = (2E - E_m)/(3E_m - 2E), \quad (5)$$

where  $E_m = m_\mu/2$  is the end-point of the positron energy spectrum. For high energy positrons the asymmetry approaches  $A = +1$  and positrons are preferentially emitted in the muon spin direction. For low energy positrons the asymmetry approaches  $A = -1/3$  and positrons are preferentially emitted opposite the muon spin direction. When integrated over the theoretical energy distribution  $N(E)$  of emitted positrons, the asymmetry is  $A = +1/3$ .

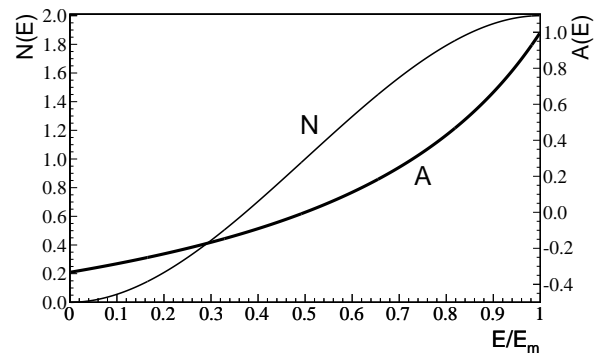


FIG. 3: The positron energy distribution  $N(E)$  and energy-dependent positron asymmetry  $A(E)$  in ordinary muon decay  $\mu^+ \rightarrow e^+ \nu_e \bar{\nu}_\mu$ .  $E_m$  is the end-point energy of the ordinary decay spectrum.

### B. Muon slowing-down in condensed matter

In the experiment a nearly 100%-longitudinally polarized surface muon beam was stopped in various target materials. The dynamics of a muon slowing-down in condensed matter has important series for the initial properties of the stopped muon ensemble in the target material.

On entering the target material the incident muons are slowed by ionization and excitation. In the final stages of slowing-down, the muons can undergo a series of electron pick-up and stripping reactions and exist as either neutral muonium atoms or charged muon “ions”. Importantly, the formation of muonium can cause the rapid depolarization of stopping muons via the large hyperfine interaction between the  $\mu/e$  magnetic moments.

The initial depolarization and magnetic species<sup>2</sup> of stopped muons are consequently dependent on the details of the muonium formation and its hydrogen-like chemical reactions in the stopping material. Empirically, large populations of diamagnetic  $\mu^+$  states are generally associated with muon stops in metals. By comparison muonium populations are less common, although their existence is well established in such materials as ice, quartz, silicon, and germanium. Any surviving polarization of stopped muon or muonium populations is potentially worrisome for lifetime measurements.

### C. Muon spin rotation in condensed matter

Following the slowing-down process the spin vectors of stopped muons will precess and relax in the local magnetic fields of the target material. This phenomenon

<sup>2</sup> The initial depolarization refers to depolarization during the slowing-down process. The magnetic species refer to diamagnetic  $\mu^+$  states and paramagnetic  $\mu^+e^-$  states with comparatively small and large magnetic moments, respectively.

is known as muon spin rotation ( $\mu$ SR).<sup>3</sup> This time-dependent muon-ensemble polarization yields, through the angular correlation between the muon spin and the positron direction, a time-dependent decay-positron angular distribution. In turn, this effect is seen—when detecting positrons in specific directions—as a geometry-dependent modulation of the exponential decay curve by the  $\mu$ SR signals.

In discussing muon spin rotation it is helpful to distinguish the cases of  $\mu$ SR in a transverse magnetic field; *i.e.*, a magnetic field perpendicular to the polarization axis, and  $\mu$ SR in a longitudinal magnetic field; *i.e.*, a field parallel to the polarization axis. Of course, in general, both effects will contribute to the time distributions of the decay positrons.

### 1. Transverse field (TF) $\mu$ SR

A transverse field  $\vec{B}$  causes the muon/muonium magnetic moment  $\vec{\mu}$  to undergo Larmor precession in the plane perpendicular to the field axis. The precession frequency is  $\omega = \mu B/2mc$  where  $m$  represents the muon/muonium mass. It yields frequencies of 13.6 kHz per Gauss for free diamagnetic muons and 1.39 MHz per Gauss for free paramagnetic muonium.<sup>4</sup>

In matter, the ensemble-averaged polarization will generally relax. One source of relaxation is the spin dephasing of the individual muons in the differing local  $B$ -fields at their stopping locations in the target material. Another source is the spin interactions between the stopped muons and the surrounding electrons and crystal lattice.

For positrons detected at an angle  $\theta_B$  relative to the  $B$ -field axis, the effects of TF  $\mu$ SR yield the time distribution depicted in Fig. 4. A common, semi-empirical representation of the time dependence of the TF  $\mu$ SR signal is

$$N(t) \propto (1 + A_2(\theta_B) e^{-t/T_2} \sin(\omega t + \phi)) e^{-t/\tau_\mu}, \quad (6)$$

where  $A_2(\theta_B)$  is the amplitude of the  $\mu$ SR signal,  $\omega$  and  $\phi$  are the frequency and the phase of the precession, and  $T_2$  is the time constant of the relaxation. Note the geometry-dependent amplitude  $A_2(\theta_B)$  is maximum for positrons emitted perpendicular to the  $B$ -field axis and zero for positrons emitted parallel to the  $B$ -field axis. Also—as shown in Fig. 4—the TF  $\mu$ SR signals of positrons emitted in opposite directions have opposite phases.

<sup>3</sup> Alternatively,  $\mu$ SR can refer to muon spin rotation, relaxation or resonance.

<sup>4</sup> The muonium ground state is a two-state system consisting of the  $F = 1$  triplet state and the  $F = 0$  singlet state. The precession frequency of triplet atoms is 1.39 MHz per Gauss. Singlet atoms are rapidly depolarized by hyperfine oscillations and therefore unobservable by  $\mu$ SR techniques.

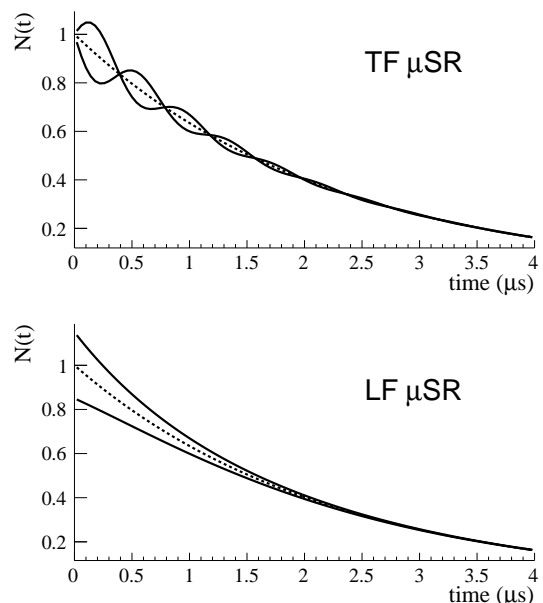


FIG. 4: Depiction of typical time spectra from TF  $\mu$ SR (upper panel) and LR  $\mu$ SR (lower panel). The paired-solid lines represent the time distributions of outgoing positrons in geometrically opposite detectors. The single-dashed line represents a positron distribution without  $\mu$ SR effects. The TF  $\mu$ SR spectrum shows both spin precession and spin relaxation whereas the LF  $\mu$ SR spectrum shows a relaxation signal but no precession signal. Note, these figures greatly exaggerate the observed effects of  $\mu$ SR in this experiment.

### 2. Longitudinal field (LF) $\mu$ SR

Because the torque  $\vec{\tau} = \vec{\mu} \times \vec{B}$  on the muon spin vanishes for a longitudinal  $B$ -field, LF  $\mu$ SR exhibits no precession signal. However, in matter the polarization will relax via the spin interactions with the surrounding electrons and the crystal lattice. Because relaxation via spin dephasing in differing  $B$ -fields is absent, the time constants for LF-relaxation are generally longer than TF-relaxation.

For positrons detected at an angle  $\theta_B$  relative to the  $B$ -field axis, the effects of LF  $\mu$ SR yield the time distribution depicted in Fig. 4. A common, semi-empirical representation of the time dependence of the LF  $\mu$ SR signal is

$$N(t) \propto (1 \pm A_1(\theta_B) e^{-t/T_1}) e^{-t/\tau_\mu}, \quad (7)$$

where  $A_1(\theta_B)$  and  $T_1$  are the amplitude and the time constant of the longitudinal relaxation. Note the geometry-dependent amplitude  $A_1(\theta_B)$  is maximum for positrons emitted along the  $B$ -field axis and zero for positrons emitted perpendicular to the  $B$ -field axis (*i.e.* the reverse of the TF-case). Again—as shown in Fig. 4—the LF  $\mu$ SR signals of positrons emitted in opposite directions have opposite signs.

### III. EXPERIMENTAL SETUP

The experiment was conducted at Paul Scherrer Institute (PSI) in Villigen, Switzerland, using a nearly 100% longitudinally polarized, surface  $\mu^+$  beam. Incoming muons were stopped in a solid target and outgoing positrons were detected by a finely-segmented, large-acceptance, scintillator array instrumented with fast-sampling waveform digitizers.

One important feature of the experimental setup was the time structure of the muon beam. This time structure or “fill cycle” consisted of a 5  $\mu$ s-long, beam-on accumulation period followed by 22  $\mu$ s-long, beam-off measurement period. The time structure was important in avoiding the need to associate decay positron with parent muons, a requirement that limited earlier experiments using continuous muon beams. Rather, the time of the decay positrons are associated with the beam-off transition.

Another important feature was a large reduction of the muon ensemble polarization via the spin precession during the accumulation period. Since muons arrive randomly during accumulation, their spins precess through different angles under the influence of the local  $B$ -field, thus dephasing the individual spins and reducing the ensemble polarization.

Additionally, the positron detector comprised a symmetric array of target-centered, geometrically-opposite, detector pairs. As  $\mu$ SR signals have equal magnitudes but opposite signs in opposite detectors (See Sec. II C), any remaining effects from  $\mu$ SR signals are largely canceled by detector symmetry.

#### A. Muon beam

The experiment used the  $\pi$ E3 beamline at the laboratory’s 590 MeV proton cyclotron. The 1.4-1.8 mA proton beam provided the intense secondary muon beam required for this high statistics experiment. The proton beam has a continuous macroscopic time structure consisting of roughly 1 ns duration proton pulses at a 50.63 MHz repetition rate.

The  $\pi$ E3 secondary beamline viewed the E-station production target in the primary proton beamline. The station comprised a 40 or 60 mm-long graphite target, which was rotated at roughly 1 Hz to prevent damage by beam heating. The rotation resulted in a slight modulation of the muon intensity.

The surface muons originate from at-rest  $\pi^+ \rightarrow \mu^+ \nu_\mu$  decays in the outer layer of the production target. The decays yield a back-to-back neutrino and positive muon with momenta 29.8 MeV/c. As a consequence of parity violation in the weak interaction, the surface muons were nearly 100% longitudinally polarized, with their spins anti-aligned to their momenta.

A schematic of the  $\pi$ E3 beamline elements from the E target station to the muon stopping target is shown in

Fig. 5. The beamline includes a fixed-element section, which views the E target station at 90 degrees to the through-going proton beam. Surface muons produced by pion decays were collected by a magnetic lens system and momentum-selected through a 60-degree, vertically oriented, dipole. Additional quadrupoles and two horizontal and vertical slit systems provide momentum- and flux-limiting apertures. A second opposing dipole and a quadrupole doublet were tuned to redirect the beam parallel to a raised experimental floor, which is roughly 6 m above the proton beam.

The customized beamline elements that follow transport muons without deflection through the uncharged electrostatic kicker and next through an  $\vec{E} \times \vec{B}$  velocity separator, which removes unwanted positrons. The beam is then focused by a quadrupole triplet through an  $x$ - $y$  slit system and then refocused by a second triplet at the stopping target. The three slit systems were adjusted to optimize the combination of beam-on intensity, momentum acceptance, and beam-off extinction.

##### 1. Electrostatic kicker

A time structure was imposed on the continuous beam using a custom-built, fast switching, electrostatic kicker [16, 17]. With the kicker high voltage off, the muons were transported straight along the beamline axis. With the kicker high voltage on, the muons were displaced vertically by 46 mm and deflected downward by 45 mrad at the kicker exit. They were then focused onto the bottom edge of the third slit system.

The kicker system includes two pairs of 75 cm-long by 20 cm-wide aluminum plates that were aligned in series with a spacing of 5 cm. The plates were positioned symmetrically above and below the beamline axis with a 12 cm gap. Collimators with apertures of 12.5 $\times$ 12 cm<sup>2</sup> were located both upstream and downstream to prevent particles reaching regions either above or below the plate gap. The plates were housed in a 60-cm diameter, 2.0-m long, cylindrical vacuum tank with high-voltage, vacuum feed-throughs.

When energized, a potential difference of 25 kV was applied between the top plates and the bottom plates (+12.5 kV was applied to the two upper plates and -12.5 kV was applied to the two lower plates with a virtual ground at the kicker mid-plane). The switching of plate voltages between ground potential and  $\pm 12.5$  kV (and vice versa) was accomplished using series circuits (“stacks”) of seventeen fast-transition, high-power, MOSFETs with each MOSFET switching 735 V. Pairs of MOSFET stacks were operated together in push-pull mode with one stack pushing the plate voltage to  $\pm 12.5$  kV and the other stack pulling the plate voltage to ground potential.

The kicker was typically operated at a cycle frequency of about 37 kHz with a 5  $\mu$ s beam-on period (plates grounded) and a 22  $\mu$ s beam-off period (plates energized).

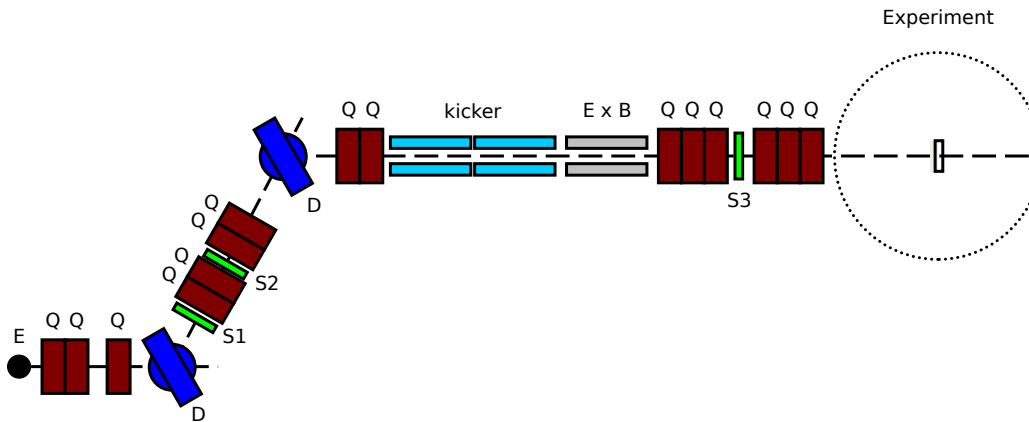


FIG. 5: Schematic view of the  $\pi E3$  beamline including the E target station, opposing vertical bending magnets (D), quadrupole focusing magnets (denoted Q), slit systems (S), electrostatic kicker,  $\vec{E} \times \vec{B}$  velocity separator, and the location of the experiment. See text for details.

The transition time between ground and  $\pm 12.5$  kV was 67 ns [16, 17]. Measurements performed during 2006 running indicated the  $\pm 12.5$  kV plate high voltage was stable to better than 300 mV. Improved measurements during 2007 running indicated a stability of better than 150 mV. For further details see Sec. VD 8.

## 2. Beam monitor

A planar, high-rate, multi-wire proportional chamber with associated readout electronics was used for both extensive beam studies prior to data taking and for periodic beam monitoring during the data taking. For the beam studies, the chamber was positioned at the stopping target location with the positron detector rolled to a downstream location. For the beam monitoring, the chamber was positioned immediately after the 150  $\mu\text{m}$ -mylar beampipe window at the downstream end of the positron detector.

The beam monitor was designed to measure the  $x$ - $y$  muon profile during the high instantaneous rates of the accumulation period and the low instantaneous rates of the measurement period. The chamber was assembled from two perpendicular anode wire planes interleaved between three high-voltage cathode planes. Each anode plane consisted of 96 tungsten anode wires of 20  $\mu\text{m}$  diameter and 1.0 mm wire spacing and each cathode plane consisted of 12.5  $\mu\text{m}$  aluminized Mylar foils held at 3.0 kV. A “fast” chamber gas of 30% isobutane and 70% tetrafluoromethane was used to handle the high rates. The beam monitor was about 98% efficient for surface muons and about 8% efficient for beam positrons.

Adjacent pairs of anode wires were connected together into 2 mm-spaced wire-pairs and read out by six, 16-channel, amplifier-discriminator boards. The resulting logic signals were recorded by a custom-built, field pro-

grammable gate array (FPGA) that combined individual hits into  $x - y$  positions and time stamps of detected particles (during the accumulation period the data was pre-scaled). The FPGA data was read out through a Struck Innovative Systeme GmbH SIS3600 32-bit VME event latch [18] by the data acquisition system.

## 3. Beam characteristics

The beam time structure is depicted in Fig. 6. The upper panel shows the muon rate over the fill cycle and indicates the 5  $\mu\text{s}$  beam-on accumulation period, 22.0  $\mu\text{s}$  beam-off measurement period, and the fast transitions between the beam-on/off states. The lower panel shows the corresponding positron rate over the fill cycle, which increases monotonically during the accumulation period and decreases exponentially during the measurement period.

The muon beam was operated at a central momentum of 28.8 MeV/c and a momentum bite of  $\sim 2.6\%$  ( $\sigma$ ). During the beam-on accumulation period, the instantaneous flux of surface muons at the stopping target was about 8 MHz in a spot size approximately  $21 \times 10 \text{ mm}^2$ . This rate yielded about 40 stopped muons per accumulation period and 15 detected positrons per measurement period. The surface muons arrive at the stopping target with their polarization tilted at a  $6^\circ$ -angle below the beamline axis. This tilt arises from spin precession in the transverse  $B$ -field of the velocity separator.

During the beam-off measurement period the instantaneous rate of surface muons was reduced by an “extinction” factor  $\epsilon \sim 900$  and the spot size was increased to about  $43 \times 32 \text{ mm}^2$ .

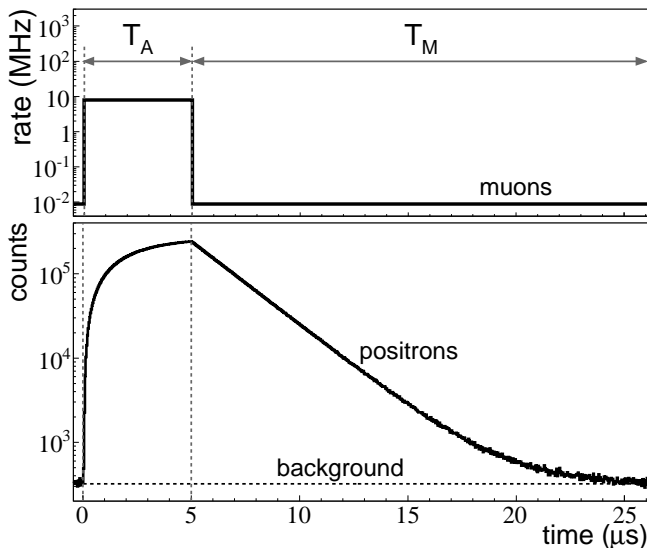


FIG. 6: Plot of the muon arrival times (upper panel) and decay positron times (lower panel) that are produced by the pulsed beam technique. The fill cycle comprises the  $T_A = 5 \mu\text{s}$  beam-on accumulation period and the  $T_M = 22 \mu\text{s}$  beam-off measurement period.

## B. Target arrangement

For the 2006/07 data taking the  $\pi\text{E3}$  beamline was extended through the positron detector with the stopping target mounted in the vacuum pipe. The in-vacuum target reduced the number of upstream muon stops compared to our 2004 commissioning experiment [14]. These stops were worrisome as their  $\mu\text{SR}$  signals are not canceled by the opposite detector sums. Such distortions were identified in Ref. [14].

The beamline extension necessitated a constriction of the vacuum pipe from 35.5-cm diameter to 20.2-cm diameter at a location 52 cm upstream of the stopping target. A hinge enabled the target to be swung into the beam path for production running and out of the beam path for beam monitoring. A collar enabled the stopping target to be rotated azimuthally about the beam axis.

Two combinations of stopping target and transverse  $B$ -fields were employed to maximize the spin dephasing of stopped muons. The first strategy used the large internal  $B$ -field of a magnetized ferromagnetic alloy target (Arnokrome-III) to rapidly dephase its population of diamagnetic muons. The second strategy used a moderate external  $B$ -field with a non-magnetic quartz crystal ( $\text{SiO}_2$ ) to rapidly dephase its population of paramagnetic muonium atoms.

To further reduce the dangers of upstream stops, the beampipe wall was also lined with Arnokrome-III ferromagnetic foil. The 0.3 mm-thick lining was arranged with its magnetization perpendicular to the beamline axis and was extended 67 cm upstream of the stopping target.

The lining dephases the ensemble-averaged polarization of upstream stops.

### 1. Arnokrome-III target setup

The Arnokrome-III (AK-3) stopping target was used in the 2006 production run. AK-3 is a ferromagnetic alloy consisting of about 30% Cr, 10% Co and 60% Fe and manufactured by Arnold Engineering Co. [19]. The disk-shaped AK-3 target had a diameter of 200 mm and thickness of 0.5 mm and was mounted on the hinged frame in the vacuum pipe at the geometrical center of the positron detector. A SRIM [20] calculation of the AK-3 target stopping power for the incident 28.8 MeV/c  $\mu^+$  beam gave a mean range of 0.17 mm and a range straggling of 0.02 mm.

The AK-3 target was magnetized in the plane of the disk. The internal  $B$ -field was approximately 0.4 T and oriented for production running with the magnetization axis to the beam left or the beam right (*i.e.* at 90 degrees to the muon polarization). In the  $\sim 0.4$  T transverse  $B$ -field the diamagnetic  $\mu^+$ 's have a  $\sim 50$  MHz precession frequency. The resulting dephasing during the accumulation period reduced the ensemble-averaged transverse polarization by roughly a factor of 700.

For further details on  $\mu\text{SR}$  effects in Arnokrome-III see Sec. V B and Ref. [21].

### 2. Quartz target setup

The quartz ( $\text{SiO}_2$ ) stopping target was used in the 2007 production run. The target was a disk-shaped, artificially grown, single crystal with a 130-mm diameter, 2.0-mm thickness that was oriented with its  $Z$ -crystallographic axis perpendicular to the disk face. The crystal was purchased from Boston Piezo-Optics Inc. [22] and grown by so-called seed-free technology to minimize crystal imperfections that possibly lead to reduced formation of muonium atoms. A SRIM [20] calculation of the quartz target stopping power for the 28.8 MeV/c muon beam gave a mean range of 0.53 mm and a range straggling of 0.03 mm.

The 130-mm diameter quartz disk was the largest diameter single crystal that was commercially available. The remaining region between the 130-mm quartz disk outer diameter and the 200-mm beam pipe inner diameter was therefore covered by a magnetized AK-3 annulus to guarantee depolarization of off-axis muon stops.

A 130-G transverse  $B$  field was used for the spin precession of the muon stops in the quartz target. The field was produced by a Halbach arrangement [23] of twenty four,  $2.5 \times 2.5 \times 2.5 \text{ cm}^3$ , neodymium magnets mounted in an aluminum ring of inner radius 14 cm, outer radius 19 cm and thickness 7.5 mm.

Note the magnet was mounted to the detector assembly rather than the beam pipe. The mounting scheme

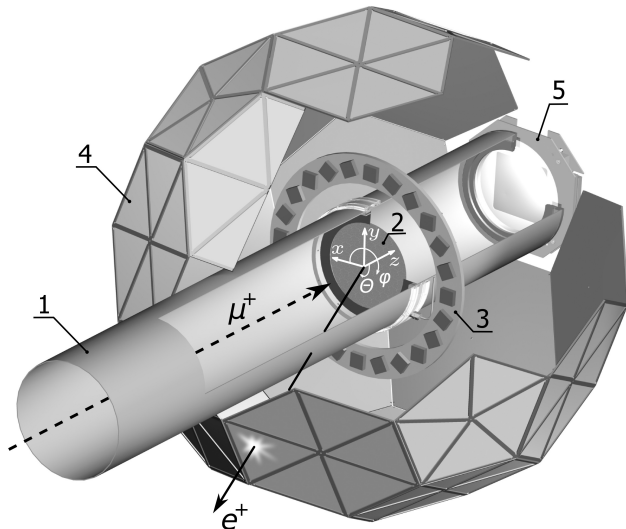


FIG. 7: Cutaway drawing of the experimental setup showing the vacuum beampipe (1), stopping target (2), Halbach magnet (3), scintillator array (4) and the beam monitor (5) at the downstream window of the beam line. Note that the Halbach magnet was not installed for the AK-3 data taking and the stopping target was rotated out of the beam path for the beam monitoring.

allowed for both its rotation about the beam axis and its inclination relative to the vertical axis. The rotation degree-of-freedom enabled the direction of the transverse  $B$  field to be varied and the inclination degree-of-freedom enabled the introduction of a longitudinal  $B$  field at the target. This setup required a careful alignment to ensure the muon polarization axis and magnetic field axis were mutually perpendicular during production running.

In the 130-G transverse magnetic field the precession frequency of muonium atoms was roughly 180 MHz and that of positive muons was roughly 1.8 MHz. The resulting dephasing during the accumulation period reduced the ensemble-averaged transverse polarization by roughly a factor of 1000 for the large paramagnetic muonium population and 25 for the diamagnetic  $\mu^+$  population.

For further details on  $\mu$ SR effects in crystal quartz see Sec. V B and Refs. [24, 25].

### C. Positron Detector

The positron detector is depicted in Fig. 7. The detector was a fast-timing, finely-segmented, large-acceptance, plastic scintillator array that was geometrically centered on the stopping target. The detector enabled an inclusive measurement of positron time and angular distributions from the muon decays in the stopping target. The detector segmentation was important in minimizing positron pileup and the detector geometry was important in han-

dling  $\mu$ SR distortions.

The detector was constructed of 170 triangle-shaped scintillator pairs arranged in a truncated icosahedral (soccer ball) geometry. Each pair comprised an inner plastic scintillator tile and outer plastic scintillator tile. The pairs were grouped into ten pentagonal enclosures (pent-houses) containing five tile-pairs and twenty hexagonal enclosures (hex-houses) containing six tile-pairs; the ten pent-houses and twenty hex-houses together forming the detector geometry. The  $\pi$ E3 beamline traversed the positron detector through one upstream pentagonal hole and one downstream pentagonal hole in the detector array.

For later reference a coordinate system with the  $z$ -axis parallel to the beam axis and the  $x(y)$ -axes in the horizontal (vertical) directions perpendicular to the beam axis is introduced. The location of detectors are specified by their polar angle  $\theta$  measured from the  $z$ -axis and their azimuthal angle  $\phi$  measured in the  $xy$ -plane (See Fig. 7). The detector arrangement yielded pairs of geometrically-opposite tiles that viewed the target with coordinates  $(\theta, \phi)$  and  $(180^\circ - \theta, \phi + 180^\circ)$ .

The triangular tiles were 3-mm thick BC-404 scintillator that produced light signals with 0.7 ns rise times and 1.8 ns fall times [26]. The tiles in hex-houses were equilateral triangles with base lengths of 15.0 cm for inner tiles and 14.0 cm for outer tiles. The tiles in pent-houses were isosceles triangles with base lengths of 15.0 cm (13.8 cm) and heights of 10.0 cm (9.5 cm) for inner (outer) tiles. The scintillator array had an inner radius of approximately 40.5 cm and subtended a solid angle of approximately 70% of  $4\pi$  steradians.

Two edges of each tile were covered with reflective tape while the remaining edge was glued to an adiabatic lightguide followed by a 29-mm diameter photomultiplier tube (PMT). The light guides and PMTs—not shown in Fig. 7—emerged radially from the geometrical center of the detector array. Two types of photomultipliers were used, with 296 tiles (eighteen hex-houses and eight pent-houses) instrumented by Photonis XP 2982 PMTs [27] and 44 tiles (two hex-houses and two pent-houses) instrumented by Electron Tube 9143 PMTs [28]. The same brands of 29-mm PMTs were used to read out geometrically-opposite detector pairs. A clip-line was used to shorten the durations of the pulses from the photomultipliers to full-widths at 20% maximum of 10 ns.

An important requirement was the accurate centering of the detector array on the stopping distribution. The detector was supported by a steel platform with an arrangement of vertical posts and horizontal rails enabling the fine adjustment of the detector horizontal and vertical coordinates. Using this arrangement, the detector array and stopping distribution were centered to better than 2 mm in each direction.



### 1. Detector operation

On average each minimally-ionizing positron (MIP) yielded a photomultiplier signal of  $\sim 70$  photo-electrons. The initial settings of the high voltages for each photomultiplier were performed by adjusting the MIP peak to correspond to one half of the 1.0 V dynamic range of the readout electronics. During data taking the gain stability was continuously monitored via the amplitude of the MIP peak and showed typical drifts of  $\sim 2$  mV per day. To compensate for long-timescale gain drifts, the PMT high voltages were adjusted on several occasions during each running period.<sup>5</sup>

The detector was designed to minimize vulnerability to gain changes. The vast majority of detected positrons were minimally ionizing particles with well-defined energy loss in scintillator tiles. By constructing the detector with two layers of scintillator tiles, and designing the detector for efficient collection of scintillation light, the resulting coincident pulses from through-going positrons were well separated from background noise.

Fig. 8 shows the distribution of hits versus the angle  $\theta$  relative to the beamline axis. The dip at 90 degrees is a consequence of the shadow of the target disk, target flange and Halbach magnet (in quartz data taking). The increase in counts either side of 90 degrees is attributed to scattering in the same components.

### D. Laser system

A laser system was used to monitor the time stability of the positron detector during the measurement period. The LN203 nitrogen laser [29] generated 337 nm wavelength, 600-ps duration, UV pulses that were split and then distributed via a fiberoptic cable to 24 scintillator tiles and one reference photomultiplier. The reference PMT was situated outside the experimental area in a location that was well-shielded from the beam-related radiation and the kicker-related electrical noise. The PMT pulse shapes corresponding to decay positrons and laser signals were similar.

In normal operations the laser system was run asynchronously with the fill cycle at a 33 Hz repetition rate. Typically the system was operated for one hour each 8-hour shift.

### E. Waveform digitizers

The PMT signals from scintillator tiles were read out via 340 channels of 450 MHz sampling-rate, 8-bit resolution, VME-based waveform digitizers (WFDs). Data

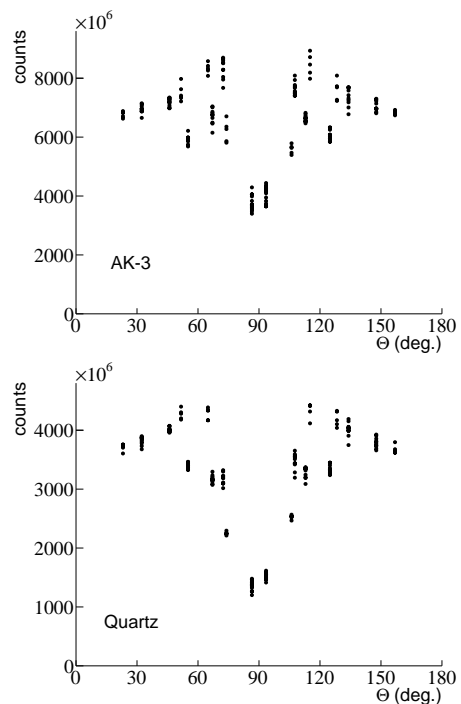


FIG. 8: Hit distribution for the 170 tile pairs versus the angle  $\theta$  relative to the beamline axis for the entire AK-3/quartz datasets. The upper panel is the hit distribution for the AK-3 setup without the Halbach magnet and the lower panel is the hit distribution for the quartz setup with the Halbach magnet. The vertical groupings with common  $\theta$ -values are tile pairs with different values of angle  $\phi$ .

from the custom-built WFDs was used to determine the times and amplitudes of the tile pulses. The latter were also used in the detailed analysis of pulse pileup and gain changes.

The WFD modules were single-slot VME-64 boards. Each module had four analog channels with 0-1 V analog input ranges, one enable input, and one clock input. The four channels of each module were used to digitize the signals from one inner-outer tile pair and its geometrically-opposite tile pair. Each enable input received a logic signal synchronized to the measurement period and each clock input received a 450 MHz sinusoidal signal distributed by the clock system.

The complete setup involved 85 WFD modules in six VME crates. The crates were located in racks on the detector platform in the experimental area. Approximately 12 meter-long, 50  $\Omega$  cables connected the PMT outputs to the WFD inputs.

Each analog input was continuously digitized by independent analog-to-digital converters (ADCs) that sample at the external clock frequency. Two field programmable gate arrays (FPGAs) controlled the data flow from the four sampling ADCs to their associated 512 kB, FIFO

<sup>5</sup> Slow gain changes over the data taking period do not interfere with the positron time distribution during the measurement period.

memories. When the enable input was present and the analog input exceeded a threshold, a time stamp, fill cycle number, and contiguous block of 24 ADC samples were written to memory. The digitized data in the WFD memories were then read out via the VME backplane. The FIFO-design permitted simultaneous read and write access to digitizer memory.

The threshold trigger that initiated storage of ADC samples was derived from a high-bandwidth voltage comparator at each analog input. Note, while the ADCs digitized at the external clock frequency  $f$ , the FPGA control electronics operated at a divided frequency  $f/4$ . Consequently, the recorded blocks of 24 ADC sample had ranges of 4-7 pre-samples preceding the “trigger” sample.

Interesting waveforms occasionally exceeded 24 ADC samples, for example when two pulses were close in time or a single pulse with a large amplitude was over threshold for a long time. Therefore, if the WFD input was over threshold during the last ADC sample of the 24-sample block, the WFD was re-triggered and recorded a continuation block of 24 additional samples.

The thresholds and offsets of each WFD channel were individually programmable via the VME interface. The WFD analog thresholds were set as low as tolerable for data taking rates. The WFD analog offsets were set to permit the recording of under-shoots following large pulses.

Due to variations in clock signal cable lengths and WFD board propagation times, the relative timing of the enable signal and the  $(f/4)$ -FPGA clock was not identical on all modules. This not only results in a time offset between the different modules, but also a time offset that steps back and forth by 4 clock ticks depending on the relative timing of the enable signal and the  $(f/4)$ -FPGA clock. Because the relative timing of the two signals changes for every measurement period, the displacements between WFD modules also change. Consequently, accumulated time histograms were actually superpositions of physical time distributions with varying proportions of the 4 clock tick displacement. Note that because no ambiguity exists between the four inputs of a single digitizer, the definition of inner-outer tile coincidences and  $\mu$ SR cancellation by opposite tile sums were unaffected. Most importantly, the determination of the lifetime was not affected by the displacements.

### F. Clock system

An Agilent E4400 function generator [30] was used for the external clock inputs of the waveform digitizer modules. The function generator derives its clock signal from a temperature-controlled crystal oscillator with a quoted short-term and long-term stability better than 0.1 ppm.

The clock was located on the detector platform in the experimental area. Its signal was amplified and split six ways to generate one copy for each WFD crate. The six copies were then amplified and passively split sixteen

ways to produce one copy of the clock signal for each WFD module.

A variation of the clock timebase that was correlated with the measurement period could cause distortions of the lifetime determination. Such effects could arise from beating between the clocks defining the digitizer sampling and kicker transitions. To eliminate this possibility the digitizer sampling frequencies and kicker transition frequencies were derived from completely independent, free running, clock systems.

The collaboration was blinded to the exact frequency of the clock until the completion of the data analysis. During data taking and data analysis the frequency was known by the collaboration to be  $451.0 \pm 0.2$  MHz. The unblinding involved first a relative unblinding of the two (2006 and 2007) datasets into commonly-blinded clock ticks and then an absolute unblinding of the entire dataset into real time units.

### G. Data acquisition

The data acquisition [31] provided the read out and data logging of the waveform digitizers and the beam monitor as well as run control, data monitoring, *etc.* The acquisition was developed using the MIDAS acquisition package [32] and the ROOT analysis package [33] on a parallel, layered array of networked Intel Xeon 2.6 GHz processors running Fedora Core 3.

To handle the high data rates and avoid any deadtime-related distortions, the readout was organized into repeating cycles of deadtime-free intervals called “data segments.” Each data segment comprised a complete, deadtime-free record of every over-threshold digitized pulse during 5000 consecutive fill cycles. Between each data segment a short deadtime of roughly 2-4 ms was imposed to complete the transactions that packaged the data and synchronized the readout. The readout scheme relied on the ability to read out and write to the WFD FIFOs simultaneously.

An important component of the acquisition system was a programmable pulser unit (PPU) that synchronized the data segments and measurement periods. The PPU was constructed from a 25 MHz Xilinx FPGA. It generated a continuous stream of fill cycles for the electrostatic kicker and a gated stream of 5000 fill cycles for the waveform digitizers. The data acquisition system initiated the beginning of each 5000 fill cycle sequence via the PPU and the PPU reported the completion of each 5000 fill cycle sequence to the data acquisition system.

The data acquisition design involved a frontend layer for data readout, a backend layer for event building and data storage, and a slow control layer for control and diagnostics. The frontend layer consisted of seven dual-core processors for the parallel readout of the six VME crates containing the waveform digitizers and a single VME crate for the beam monitor readout. Each VME crate was read out using a Struck Innovative Systeme

GmbH SIS3100/1100 PCI-to-VME interface [34]. The frontend programs incorporated lossless compression of raw data using Huffman coding [35, 36] as implemented in ZLIB [37].

The backend layer received data fragments asynchronously from the frontend layer via a 1 Gb Ethernet network. The fragments were assembled into complete events that comprised all the recorded pulses during the data segment. These events were then written to a RAID-10 disk array and finally migrated to 400 GB LTO3 tapes.

The slow control layer was responsible for operation and monitoring of various instruments such as high voltage supplies, beamline magnet supplies, temperature monitors, and  $B$ -field monitors. Slow control data was read out periodically with one copy written to the main datastream and another copy written to an online database.

Lastly, an online analysis layer was responsible for ensuring data quality. The online analyzer received data “as available” to avoid introducing any unnecessary dead-times into data readout. As well as recording basic quantities such as run start/stop times and event statistics, the online analysis layer determined quantities such as detector gains and fitted lifetimes. These run-by-run quantities were stored in an online database that provided a comprehensive record of data taking and enabled a straightforward monitoring of data integrity.

#### IV. DATA PREPARATION

The procedure to obtain the positron time histograms from digitized scintillator pulses involves first determining the various parameters of individual tile pulses and then constructing the coincidences between inner-outer tile hits. Finally, the accumulated histograms of coincidence times are corrected for systematic effects including pulse pileup and gain changes.

The data obtained from the 2006 production run (R06) using the AK-3 target has  $1.1 \times 10^{12}$  decay positrons and the data obtained from the 2007 production run (R07) using the quartz target has  $5.4 \times 10^{11}$  decay positrons. The R06(R07) data were recorded in runs of duration 2(10) minutes and size 2(10) GBytes, each containing about  $4 \times 10^7 (2 \times 10^8)$  positrons. In total they yielded about 130 terabytes of raw data.

As listed in Table I, the R06/R07 production data are divided into subsets with different orientations of the magnetic field relative to the beam axis and different positions of the geometrical center of the detector relative to the surveyed intersection of the beam axis with the target disk. These subsets are important for consistency checks and systematic studies.

Shorter systematics datasets were also collected. Examples of systematics datasets omitted in the final statistics are (i) magnet orientations that introduced large longitudinal  $B$  fields at the stopping target, (ii) detec-

tor alignments that introduced large geometrical asymmetries between opposite tile pairs, and (iii) shorter accumulation periods that decreased the spin dephasing. Short measurements taken every shift with low rates of laser pulses illuminating a sub-set of scintillator tiles are included in the final statistics.

The analysis was conducted using the 88-teraflop ABE cluster and mass storage system (MSS) at the National Center for Supercomputing Applications (NCSA) [38]. The processing of digitized waveforms into time histograms took roughly 60,000 CPU-hours for each dataset.

TABLE I: Summary of R06/R07 production datasets indicating the subsets with different magnetic field orientations and detector alignments. The magnetic field orientation is denoted L for beam-left and R for beam-right. The detector position represents the different coordinates of the geometrical center of the detector relative to the surveyed intersection of the beam axis with the target disk.

data subset	detector position [cm]			magnet orientation	detected positrons
	$x$	$y$	$z$		
R06-A	0	0	0	L	$6.1 \times 10^{11}$
R06-B	0	0	0	R	$5.0 \times 10^{11}$
R07-A	0	0	0	L	$2.1 \times 10^{11}$
R07-B	0	0	0	R	$2.4 \times 10^{11}$
R07-C	1.0	-1	0	L	$3.2 \times 10^{10}$
R07-D	0.5	-1	0	L	$1.4 \times 10^{10}$
R07-E	0.5	0	0	L	$3.0 \times 10^{10}$
R07-F	0.5	-0.5	0	R	$1.8 \times 10^{10}$

Prior to analysis, a number of checks of data integrity were performed for occasional hardware or software failures. The checks ensured no loss or corruption of data between the digitizer electronics and the analysis code. About 1.2% of runs were rejected by integrity checks.

#### A. Pulse fitting

The time and amplitude of pulses are determined by least square fits to the individual digitized waveforms of each scintillator pulse. The procedure involves fitting a relatively high-resolution standard waveform (0.022 ns sampling-interval) to a relatively low-resolution individual waveform (2.2 ns sampling-interval) and it assumes the pulse shape is independent of pulse amplitude.

##### 1. Pulse templates

The high-resolution standard waveforms (pulse templates) are constructed by combining a large number

of 450 MHz sampling-rate, single-pulse, digitized waveforms. One template is derived for each scintillator tile using single-pulse waveforms with peak amplitudes of 120-220 ADC counts.

The template construction relies on the independence of the positron arrival times and the digitizer clock phase, which implies a uniform time distribution of pulse maxima across the sub-sample time intervals between consecutive clock ticks (c.t.). The waveforms of individual pulses thus correspond to displaced sets of samples from the same underlying pulse shape. This makes it possible to reconstruct a high-resolution pulse template from many time-adjusted low-resolution waveforms via the computation of the aforementioned sub-sample time interval for each individual waveform.

The procedure for computing the sub-sample time intervals of individual waveforms follows Ref. [39]. It involves first calculating a sub-sample pseudo-time  $t'$  for each digitized waveform

$$t' = \frac{2}{\pi} \tan^{-1} \left( \frac{S_m - S_{m-1}}{S_m - S_{m+1}} \right) \quad (8)$$

from the three consecutive ADC samples  $S_{m-1}$ ,  $S_m$  and  $S_{m+1}$  centered on the maximum sample  $S_m$ . Then, using the measured distribution of pseudo-times  $t'$  and the uniform distribution of true times  $t$ , the pseudo-time is mapped to true time.

Finally, using the true times the individual waveforms are time-aligned and superimposed in the construction of the pulse template for each scintillator tile. Fig. 9 (upper panel) shows a representative pulse template for an individual scintillator tile.

## 2. Fitting algorithm

The pulse fitting algorithm fits pulse templates to individual waveforms so as to minimize

$$D = \sum^{N \text{ samples}} \left[ S_i - P - \sum^{n \text{ templates}} A_j f_i(t_j) \right]^2 \quad (9)$$

where  $S_i$  are the  $N$  samples of the digitized waveform and  $f_i(t_j)$  are the  $n$  templates of the scintillator pulses. The free parameters in Eqn. 9 comprise the time  $t_j$  and amplitude  $A_j$  of each scintillator pulse and an assumed constant pedestal,  $P$ . In minimizing the quantity  $D$ , all samples are equally weighted, except for underflows or overflows which were excluded from the computation. The equal weighting of ADC samples is discussed further in Sec. VD 2.

Given that the datasets contain  $\sim 10^{12}$  pulses, the algorithm for fitting is optimized for speed and robustness. As the probability of two pulses on one waveform is roughly 1%, the algorithm first tries to fit a single template to each waveform. Because the fit-function  $P + A_1 f_i(t_1)$  is linear in  $A_1$  and  $P$ , the minimum of  $D$

is found by a one-dimensional search on the non-linear parameter  $t_1$ , with the other parameters calculated from their partial derivatives at the fit minimum. This one-dimensional search is performed by parabolic minimization using Brent's Method [40].

If the quality of this fit is not acceptable (as indicated by a search for further pulses in the residuals) the algorithm then tries to improve the fit by adding pulses, removing pulses and using more sophisticated, time-consuming,  $\chi^2$ -minimization procedures. In fitting a waveform to  $n > 1$  pulses, the fitter first tries an  $n$ -dimensional search on the pulse times  $t_i$  using the Minuit minimization code [41] with the remaining parameters calculated from the aforementioned partial derivatives. If the  $\chi^2$  exceeds a maximum value, the fitter attempts a  $2n+1$  dimensional search over all fit parameters. The fitter continues to add pulses or remove pulses until either (i) the residuals indicate no evidence for further pulses or (ii) ten attempts to fit  $n > 1$  pulses are completed.

During fitting, the algorithm will reject any pulses with amplitudes  $A_j$  less than 35 ADC counts, times  $t_j$  outside the waveform boundaries, or times  $t_j$  within three samples of other pulses. When no pulses are found, the pulse fitter calculates an amplitude-weighted time of all ADC samples.

Sample fits to digitized "islands" containing a single pulse and two overlapping pulses are shown in Fig. 9. The digitized waveforms were overwhelmingly single pulse islands with fractional contributions of roughly  $1 \times 10^{-2}$  from two pulse islands and roughly  $7 \times 10^{-4}$  from zero pulse islands.

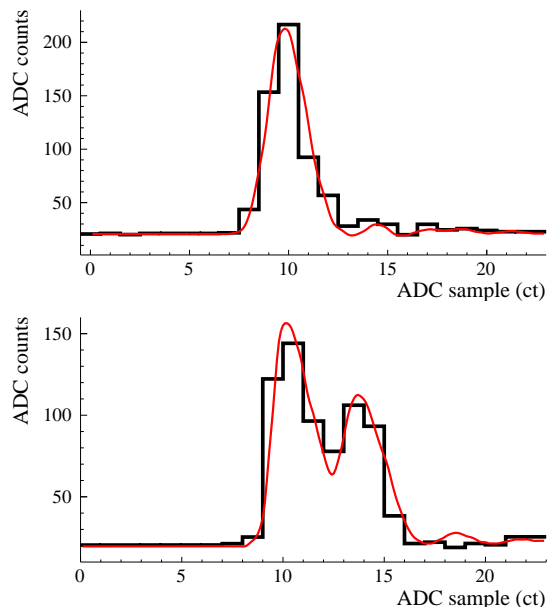


FIG. 9: Examples of the digitized waveforms and the corresponding fit results for a single pulse (upper panel) and two overlapping pulses (lower panel). The waveforms are indicated by the histogram and the fit function by the curve.

## B. Hit definition

Two cuts are applied before constructing the coincidences; one defining an unambiguous software threshold for pulses and another defining an unambiguous software deadline between hits. The construction of coincidence datasets with different threshold and deadline settings is important for studying such effects as pulse pileup and gain variations.

A typical pulse amplitude spectrum for an individual scintillator tile is plotted in Fig. 10. It shows a broad peak due to decay positrons at  $\sim 120$  ADC units and a rising background due to noise pulses below  $\sim 50$  ADC units. As shown in Fig. 10, these distributions are fit to the convolution of a Landau function and a Gaussian peak plus a linear background term. The fit-function minimum defines the normal amplitude threshold  $A_{thr}$ , corresponding to the valley between the low-energy noise and the positron MIP peak.

This threshold is re-calculated every 100(10) runs in R06(R07) data taking in order to account for the observed, long-timescale drifts in the detector gains over the data-taking period. Additional datasets, with higher thresholds of  $A_{thr} + 20$ ,  $A_{thr} + 30$  and  $A_{thr} + 40$ , are processed for studying the effects of gain variations during the measurement period.

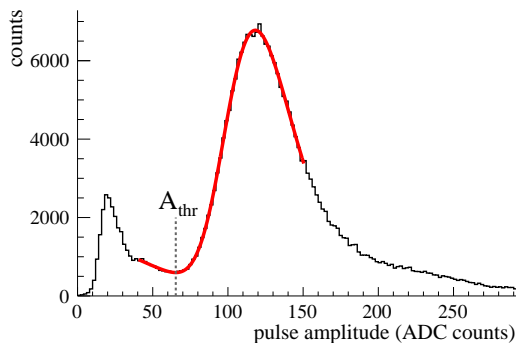


FIG. 10: Representative pulse amplitude distribution for an individual scintillator tile. The histogram represents the measured data and the smooth curve the fit function (see text for details). The fit-function minimum defines the normal amplitude threshold  $A_{thr}$  for each scintillator tile.

The pileup of positrons within the instrumental deadline distorts the measured time distribution. Specifically, when two positrons are separated by  $>3$  c.t. (6.7 ns), the corresponding pulses are cleanly resolved by the fitting algorithm. However, when two positrons are separated by  $<3$  c.t. (6.7 ns), the algorithm cannot reliably discriminate the overlapping pulses.<sup>6</sup>

<sup>6</sup> Subsequently, an ADT of  $\geq 6$  c.t. (13.3 ns) is used to avoid any re-triggering on the trailing-edges of the scintillator pulses.

To explicitly define the minimum resolving-time between neighboring pulses, a software deadline following above-threshold hits is introduced. It rejects any additional hits within an artificial deadline (ADT). A detailed study of pileup distortions with different ADTs of 5-68 c.t. (11–151 ns) was made (see Sec. IV C 1).

A typical inner-outer pair time difference spectrum is plotted in Fig. 11. It shows a sharp coincidence peak from through-going positrons with a time resolution of 0.55 ns ( $1\sigma$ ). The time offsets between inner-outer pairs, originating from differences in PMT voltages, cable lengths, and light guide configurations, are determined by a Gaussian fit to each inner-outer time difference histogram. A run-by-run table of timing offsets is used to account for changes of the offsets during the data-taking.

The individual tile hits are then sorted into datasets of inner-outer coincidences, inner singles, and outer singles. The inner-outer coincidences for each tile pair are identified using a coincidence window of  $\pm 1$  ADT.<sup>7</sup> The coincidence time is defined as the time corresponding to the later hit of the inner-outer pair.

In the unlikely case that two combinations of coincidence pairs are found within  $\pm 1$  ADT—for example when one outer hit falls between two inner hits with mutual separations of 1-2 ADT—the earlier combination of hits defines the inner-outer coincidence (this reduces the sensitivity to coincidences originating from photomultiplier “ringing”). Such circumstances yield one coincidence hit and one single hit.

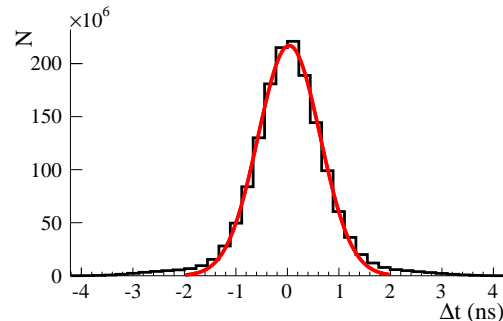


FIG. 11: Representative time difference distribution for a single inner-outer pair. The histogram is the measured distribution and the curve is the Gaussian fit. The observed timing jitter between inner-outer pairs is typically 0.55 ns ( $1\sigma$ ).

Finally, the sorted datasets of coincidence hits and singles hits are used to fill per-run, per tile-pair, histograms of inner singles, outer singles and inner-outer coincidence times.

<sup>7</sup> Using the same coincidence window and artificial deadline simplifies the pileup correction procedure. It, however, does increase the contribution from accidental coincidences between unrelated singles hits in inner-outer tile pairs.

### C. Histogram corrections

Before fitting the time histograms to extract the muon lifetime, several corrections are applied. The largest corrections account for time-dependent distortions arising from pileup of the decay positrons and variations of the detector gains. In addition, the statistical uncertainties on histogram bin contents are corrected for multiple tile-pair hits originating from positron scattering, positron annihilation and cosmic-rays.

#### 1. Pulse-pileup correction

In filling the histograms, a well-defined, fixed-length, artificial deadtime is applied so that subsequent detector hits within the ADT of an earlier detector hit are not used. Consequently, the measured time distribution corresponding to a parent time distribution  $N(t) \propto e^{-t/\tau_\mu}$  will be

$$N'(t) \propto e^{-t/\tau_\mu} - r e^{-2t/\tau} + \dots \quad (10)$$

where the second term represents the leading-order pileup losses having a magnitude  $r$  that depends on the beam rate and the ADT.

The procedure for correcting pileup takes advantage of the time structure of the incident beam. The pileup losses are statistically recovered using so-called “shadow windows”, by replacing the lost hits in each measurement period with measured hits at equivalent times in neighboring measurement periods.

To illustrate the method, consider the case of leading-order pileup, where a second hit within the artificial deadtime is lost. To correct this loss, if a hit is observed at a time  $t_i$  in a fill  $j$  (denoted the “trigger” hit), a hit is searched for in an interval  $t_i \rightarrow t_i + \text{ADT}$  in the fill  $j + 1$  (denoted the “shadow” hit). Adding the resulting histogram of shadow hit times to the original histogram of trigger hit times thereby statistically restores the hits lost to leading-order pileup.

The leading-order pileup correction for  $\text{ADT} = 6$  c.t. (13.3 ns) is depicted in Fig. 12 (curve 2). The correction ranges from roughly  $10^{-3}$  at the start of the measurement period to roughly  $10^{-7}$  at the end of the measurement period.

The leading-order correction is insufficient to entirely account for pileup effects. As the shadow windows have a width equal to the ADT, they contain either zero hits or one hit. Consequently—at the level of the higher-order pileup—the leading order pile-up is over-corrected and the higher-order pile-up is under-corrected by the shadow window (as  $> 1$  hits in the shadow window are treated as 1 hit in the shadow window).

To correct second-order pileup, if a shadow hit is found in the shadow window applied to fill  $j+1$ , another shadow hit is searched for in a second shadow window applied to

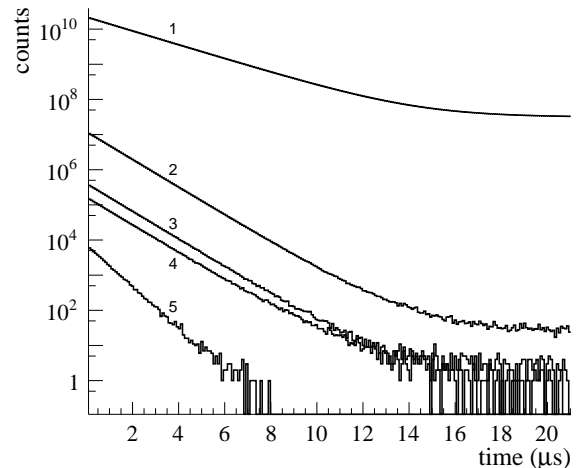


FIG. 12: Representative time distributions for the trigger hits before the pileup correction (curve 1) and corrections accounting for leading-order pileup (curve 2), extended pileup (curve 3), accidental coincidences (curve 4) and second-order pileup (curve 5). These histograms correspond to an artificial deadtime  $\text{ADT} = 6$  c.t. (13.3 ns).

fill  $j + 2$ .<sup>8</sup>

The second-order pileup contribution for  $\text{ADT} = 6$  c.t. is also depicted in Fig. 12 (curve 5). Its contribution is roughly  $10^{-6}$  at the start of the measurement period and is completely negligible by the end of the measurement period. For a parent time distribution  $e^{-t/\tau}$ , the second-order pileup time distribution has a time dependence  $e^{-3t/\tau}$  and an amplitude that increases quadratically with artificial deadtime.

The pileup corrections described above assume the absence of the  $\sigma \sim 0.5$  ns timing jitter between the inner and outer tile hits. This timing jitter causes additional pileup losses of inner-outer coincidences when one hit is lost but the other hit is not (recall the ADT is applied before defining the coincidence). This “extended” pileup is measured by searching for single tile hits within the jitter of the trailing edge of each shadow window.

The extended pileup correction is plotted in Fig. 12 (curve 3). Its contribution is roughly  $10^{-5}$  at the start of the measurement period and is completely negligible by the end of the measurement period. For a parent time distribution  $e^{-t/\tau}$ , the extended pileup time distribution has the time dependence  $e^{-2t/\tau}$  and an amplitude that is ADT-independent (at least for  $\text{ADT} \ll \tau$ ).

Random coincidences between unrelated singles hits can cause accidental coincidence hits. They can originate from muon decays, environmental backgrounds, and elec-

<sup>8</sup> In practice, the shadow windows are applied using a five-fill ring buffer, with fill 1 being corrected by fills 2 and 4, fill 2 being corrected by fills 3 and 5, and finally fill 5 being corrected by fills 1 and 3.

tronic noise. A significant number of inner tile hits without outer tile hits occur because inner tiles are slightly larger than outer tiles. Overall about 27% of inner hits are singles and about 3% of outer hits are singles.

A shadow window technique is also used to correct for accidental inner-outer coincidences. An inner singles hit at time  $t_i$  in the trigger fill initiates a search for an outer singles hit at time  $t_i \rightarrow t_i + \text{ADT}$  in the shadow fill.

The measured contribution of accidental coincidences is depicted in Fig. 12 (curve 4). It ranges from roughly  $10^{-5}$  at the start of the measurement period and is negligible by the end of the measurement period. For a parent singles time distribution  $e^{-t/\tau}$ , the accidental coincidence time distribution has a time dependence  $e^{-2t/\tau}$  and an amplitude that increases linearly with artificial deadtime.

A Monte Carlo (MC) simulation is performed to verify the procedure for correcting pileup. The MC generates a sequence of beam cycles with tile hits from parent time distributions that reproduce the observed rates of coincidence hits and singles hits from muon decays and background sources. The simulation also incorporates the measured timing jitter between inner-outer pairs.

The simulated data are analyzed using the same procedures as the measured data, *i.e.*, applying the artificial deadtime, forming the inner-outer coincidences, and accumulating the histograms of trigger hits and shadow hits. The simulated trigger hit time distributions are corrected with the simulated shadow hit time distributions and are found to reproduce the parent hit time distribution. In particular, the “true” lifetime in the absence of pileup effects, accidental coincidences and timing jitter, and corrected lifetime after the accounting for pileup effects, accidental coincidences and timing jitter, are in good agreement. The lifetimes derived for ADT ranges of 5–68 c.t. (11–151 ns) are in agreement to a precision  $\pm 0.1$  ppm (see Fig. 13).

## 2. Gain variation correction

When applying deadtimes, constructing coincidences and filling histograms, only hits with amplitudes that exceed the threshold  $A_{thr}$  are used. If the detector gain changes over the measurement period, then the time histogram will be distorted, either by additional hits rising above the amplitude cut or by additional hits falling below the amplitude cut.<sup>9</sup>

The detector gain versus measurement time is obtained by accumulating a sequence of pulse amplitude spectra corresponding to consecutive, 220 ns-wide, time windows over the entire measurement period. Because the amplitude distributions for decay positrons and cosmic rays are different, and the relative proportion of decay positrons

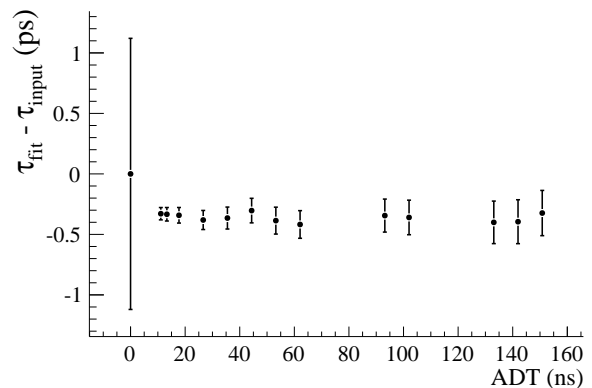


FIG. 13: Fitted muon lifetime versus artificial deadtime obtained from an analysis of a Monte-Carlo simulation of pileup effects, accidental coincidences and timing jitter. The simulated data are analyzed using the same software and methods as measured data. The fitted lifetime is ADT-independent to better than 0.1 ppm and in statistical agreement with the “true” lifetime depicted at the location ADT = 0. The error bars on the ADT > 0 points correspond to the statistical variations allowed by the ADT correction. The error bar on the ADT = 0 point corresponds to the statistical variation allowed between the “true” lifetime that omits the pulse pileup, accidental coincidences and timing jitter, and the ADT > 0 lifetimes that correct for pulse pileup, accidental coincidences and timing jitter.

and cosmic rays is time dependent, the positron distributions are obtained from measured distributions by subtracting the cosmic-ray distributions. The subtraction uses the measured cosmic-ray distribution in the last 220 ns time window of the measurement period.

The positron amplitude distributions are then fit to a convolution of a Landau energy loss distribution and a Gaussian instrumental resolution to derive the Landau most-probable-value (MPV) versus measurement time. In the absence of instabilities the MPV would be independent of the measurement time.

Fig. 14—which plots MPV versus measurement time for scintillator tiles sub-divided by photomultiplier type—indicates a gain variation of roughly  $5 \times 10^{-4}$  over the measurement period. One feature, which appears independent of PMT type, is an oscillation of the gain over the first microseconds of the measurement period. Another feature, which appears different for PMT types, is a drift of the gain over the entire duration of the measurement period.

A gain variation during the measurement period will distort the extracted lifetime. The change in the counts exceeding the amplitude cut,  $\Delta N$ , and the change in the MPV of the amplitude distribution,  $\Delta A_{MPV}$ , are related by

$$\Delta N = 2 N_{thr} \Delta A_{MPV} (A_{thr}/A_{MPV}) \quad (11)$$

<sup>9</sup> Because the threshold  $A_{thr}$  is applied to pedestal-subtracted amplitudes the time histogram is not distorted by pedestal variations.

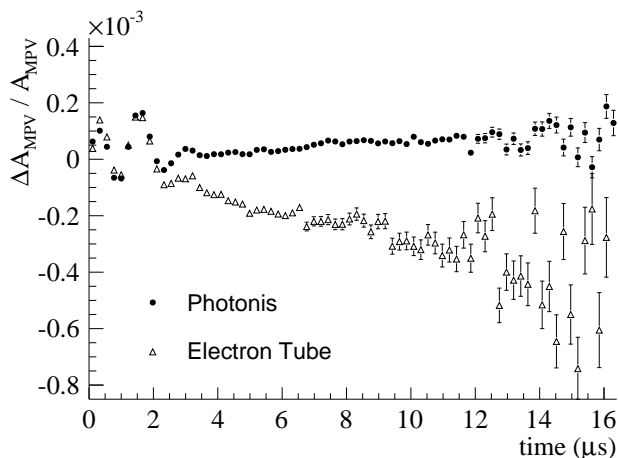


FIG. 14: Fractional MPV change versus the hit time in the measurement period. The solid circles correspond to the amplitude variation of tiles with Photonis PMTs and the open triangles correspond to the amplitude variation of tiles with Electron Tube PMTs.

where  $N_{thr}$  is the counts in the histogram bin corresponding to the amplitude cut, and  $\Delta A_{MPV}$  ( $A_{thr}/A_{MPV}$ ) is the inferred change in the amplitude cut via a scaling of the measured change in the Landau MPV. The factor of 2 in Eqn. 11 arises as gain changes of both inner and outer tiles can alter the above-threshold coincidences.

Using the measured MPV versus measurement time and Eqn. 11, the time histograms are then corrected for gain variations. In one approach, the measured  $\Delta A_{MPV}$  distribution is converted to a hit variation  $\Delta N$  and used to subtract (add) the extra (lost) hits from gain changes. In another approach, the MPV distribution is first fit to an empirical function describing the gain changes. This function is then converted from MPV versus measurement time to hits versus measurement time and used to make the gain correction (this approach is helpful in understanding the sensitivity of  $\tau_\mu$  to oscillations and drifts). The gain corrections are applied separately to Electron Tube and Photonis PMTs.

Gain instabilities during the measurement period are identified with the photomultipliers and the readout electronics.

- (i) The gain oscillations in Fig. 14 originate from electronics instabilities due to fan-out modules that distribute the measurement period start signals to all waveform digitizer modules. The oscillations are reproducible in bench tests of waveform digitizers and are observed in all channels of all waveform digitizer modules in all VME crates.
- (ii) The gain drift in Fig. 14 is dependent on PMT type. To understand this effect, amplitude distributions corresponding to different time intervals between consecutive detector hits are examined. The time dependencies of the Landau MPV ver-

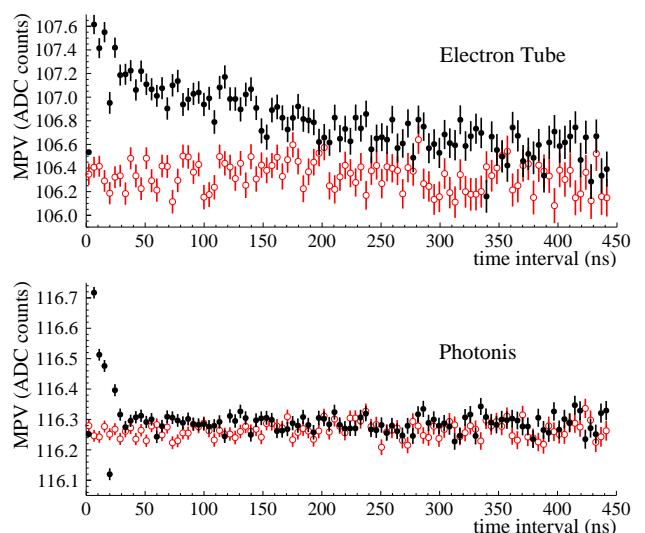


FIG. 15: Time dependencies of the Landau MPV versus the time interval after a preceding pulse for representative groups of Electron Tube PMTs (upper panel) and Photonis PMTs (lower panel). The black data points correspond to time intervals between two hits in the same tile pair and the same fill cycle. The red data points correspond to time intervals between two hits in the same tile pair but two neighboring fill cycles. The red points show no evidence of longer term effects from gain variations between neighboring fills.

sus the elapsed time after the preceding pulse are plotted in Fig. 15 for each PMT-type. The Photonis PMTs show a relatively short-timescale effect of duration  $\sim 25$  ns and fractional gain change  $\sim 1\%$ . The Electron Tube PMTs show a relatively long-timescale effect of duration  $\sim 250$  ns and fractional gain change  $\sim 1\%$ . Because rates change with measurement time, these analog pileup effects contribute to the gain drift during the measurement period.

The pileup effect in item (ii) is distinct from the “digital” pileup associated with the artificial deadtime that was discussed earlier in Sec. IV C 1. Effect (ii) is not corrected by the shadow window technique.

### 3. Hit multiplicity correction

The final correction accounts for multiple coincidence hits arising from single parent events. For example, a through-going cosmic ray or scattered decay positron may yield  $>1$  coincidence hits. Consequently, the number of coincidence hits in the time histograms exceeds the number of independent events populating the time histograms.

To correctly account for statistical uncertainties, the separate time histograms of multiplicity-one coincidences



and multiplicity-two coincidences are accumulated.<sup>10</sup> These histograms are then fit to obtain the relative contribution of multiplicity-one and -two coincidences to the decay curve and the time-independent background (the two contributions have different origins and different multiplicities). Denoting the multiplicity one and two contributions as  $N_1$  and  $N_2$  (decay term) and  $C_1$  and  $C_2$  (background term), the ratio of independent events to coincident hits versus measurement time is

$$R = \frac{(N_1 + N_2)e^{-t/\tau_\mu} + (C_1 + C_2)}{(N_1 + 2N_2)e^{-t/\tau_\mu} + (C_1 + 2C_2)}. \quad (12)$$

The ratio  $R$  decreases from 0.97 at early times (*i.e.*, a  $\sim 3\%$  contribution of multiplicity-two hits) to 0.96 at late times (*i.e.*, a  $\sim 4\%$  contribution of multiplicity-two hits). To account for events with multiplicities  $>1$  the Poisson uncertainties on bin contents are inflated by  $1/\sqrt{R}$ . Note that this correction only affects the uncertainty on the lifetime and the  $\chi^2$  of the fit—not the value of the lifetime.

## V. LIFETIME ANALYSIS

The extraction of the positive muon lifetime from fits to the positron time histograms is described next. Supplementary studies of transverse field and longitudinal field  $\mu$ SR in AK-3 and quartz and various checks on data integrity are presented. Systematic corrections and systematic uncertainties that arise from  $\mu$ SR effects, pulse pileup, gain changes, and time-dependent backgrounds are described.

### A. Fitting procedures in AK-3 and quartz

The muon lifetime is obtained by fitting the time histograms of inner-outer coincidences. In principle, each pileup-corrected, gain-corrected tile-pair time distribution can be fit to the elementary function,

$$N(t) = Ne^{-t/\tau_\mu} + C \quad (13)$$

where  $\tau_\mu$  is the muon lifetime,  $N$  is a normalization constant and  $C$  represents the flat background. In practice, distortions arising from residual  $\mu$ SR effects must be considered. Separate fitting strategies are employed for AK-3 and quartz because the specific characteristics of their  $\mu$ SR signals are different. Most important is the absence (presence) in AK-3 (quartz) of discernible  $\mu$ SR effects in the individual tile-pair time histograms.

<sup>10</sup> Multiplicity-one coincidences are defined as one inner-outer hit in an 8 c.t. (17.7 ns) interval and multiplicity-two coincidences are defined as two inner-outer hits in an 8 c.t. (17.7 ns) interval. The effects of higher multiplicities are negligible.

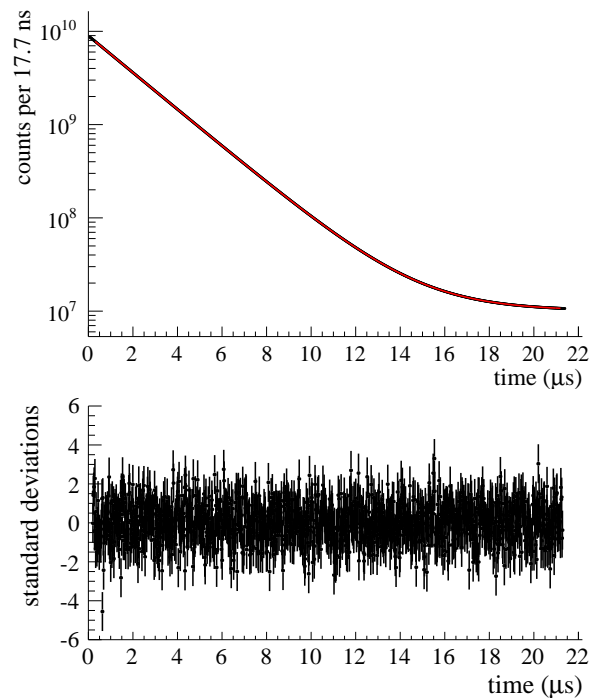


FIG. 16: Three-parameter fit to the entire AK-3 dataset. The upper panel shows both the measured data and the fit function and the lower panel shows the normalized residuals between the data points and the fit function.

In all cases the benchmark fits use histograms prepared with an artificial deadtime 6 c.t. (13.3 ns) and the aforementioned correction procedures for pulse-pileup, gain changes and hit-multiplicities. The nominal fit start and stop times are  $t_{start} = 0.22 \mu\text{s}$  and  $t_{stop} = 21.12 \mu\text{s}$ , a range which begins and ends at a safe interval from the beam (kicker) transitions. However, the results do not include the extrapolation to ADT = 0 discussed in Sec. VD 1 below.

#### 1. Fit to the AK-3 data

A simple fit method is used for AK-3 production data. The summed tile-pair time histogram is fit to Eqn. 13, the lifetime result thereby relying on sufficient cancellation of  $\mu$ SR effects by spin dephasing, target choice and detector geometry.

The benchmark fit to the entire AK-3 dataset (R06-A + R06-B) with Eqn. 13 is plotted in Fig. 16. The extracted lifetime is  $\tau_\mu = 2\,196\,980.1 \pm 2.5$  ps. Both the fit  $\chi^2/\text{dof}$  of 1224/1185 and the distribution of the residuals between the data points and the fit function indicate a reasonable fit and no evidence of any distortions such as uncanceled  $\mu$ SR effects, mis-corrected pulse pileup or time-dependent backgrounds.

The lifetime results for the benchmark fits to the separate R06-A and R06-B datasets of  $\tau_\mu = 2\,196\,979.2 \pm$

3.4 ps and  $\tau_\mu = 2\,196\,981.3 \pm 3.8$  ps are in good agreement (the two datasets have reversed  $B$ -fields). The  $\chi^2/\text{dof}$  of the fits and the distributions of the residuals are also acceptable.

## 2. Fit to the quartz data

A more detailed approach to LF/TF  $\mu\text{SR}$  effects is used to extract the lifetime from quartz data. First, geometry-dependent effective lifetimes are extracted for each tile-pair from fits using a modified version of Eqn. 13 accounting for transverse-field precession. Then,  $\tau_\mu$  is extracted from the effective lifetimes via a fit function that accounts for geometry-dependent longitudinal-field relaxation. Together these two steps account for all observed features of TF/LF  $\mu\text{SR}$  in quartz.

In step one the 170 time histograms of all tile-pairs are fit to

$$N(t) = N e^{-t/\tau_{\text{eff}}} [1 + f(t)] + C \quad (14)$$

where  $\tau_{\text{eff}}$ ,  $N$  and  $C$  are the effective lifetime, normalization constant and background amplitude, respectively. The additional term  $f(t)$  accounts for the TF  $\mu\text{SR}$  signal according to

$$f(t) = A \sin \theta_B P_2 e^{-t/T_2} \sin(\omega t + \phi) \quad (15)$$

where  $P_2$ ,  $T_2$ ,  $\omega$  and  $\phi$  are the initial polarization, relaxation constant, angular frequency and phase of the TF  $\mu\text{SR}$  signal. The quantity  $A$  is the asymmetry parameter of the  $e^+$ -angular distribution and the angle  $\theta_B$  is the tile coordinate relative to the  $B$ -field axis. The product  $A \sin \theta_B$  determines the geometry-dependent amplitude of the TF  $\mu\text{SR}$  signal in each tile pair (see Sec. II C).

A 5-parameter fit using Eqn. 14 is employed to extract the 170 tile-pair effective lifetimes. The parameters  $\tau_{\text{eff}}$ ,  $N$ ,  $P_2$ ,  $\phi$  and  $C$  are varied. The parameters  $T_2$  and  $\omega$  are fixed to the weighted averages of their best-fit values from an initial 7-parameter fit to a sub-set of tile-pairs having large TF signals. The asymmetry parameter is always set at  $A = +1/3$ . Any difference between this theoretical energy-integrated asymmetry and the detector efficiency-weighted asymmetry is subsumed into  $P_2$ .

In step two the distribution of effective lifetimes versus tile-pair coordinates  $(\theta_B, \phi_B)$  about the  $B$ -field axis is fit to

$$\tau_{\text{eff}}(\theta_B, \phi_B) = \tau_\mu (1 + \delta(\theta_B, \phi_B)) \quad (16)$$

where  $\tau_\mu$  is the true muon lifetime and  $\delta(\theta_B, \phi_B)$  is the tile-coordinate-dependent lifetime shift due to LF  $\mu\text{SR}$  effects. The scheme for incorporating LF  $\mu\text{SR}$ , which

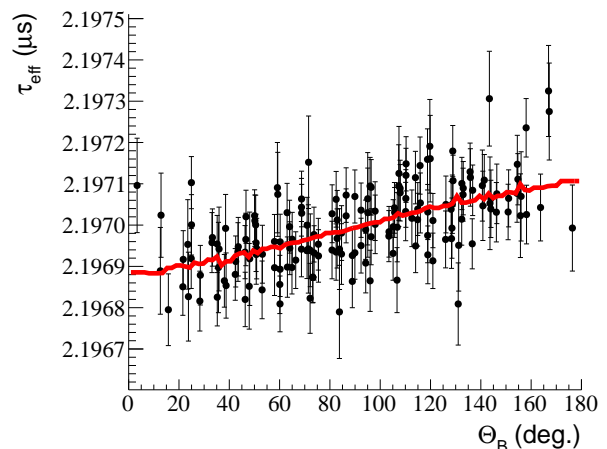


FIG. 17: Effective muon lifetime  $\tau_{\text{eff}}$  versus tile coordinate  $\theta_B$  relative to the  $B$ -field axis. The data points are the 170 individual effective lifetime measurements and the solid curve is the effective lifetime fit from Eqn. 14. The small irregularities in the solid curve arise from the  $\phi_B$ -dependence of the asymmetry parameter  $A$ .

holds when  $T_1/P_1 \gg \tau_\mu$ ,<sup>11</sup> yields

$$\delta(\theta_B, \phi_B) = \tau_\mu \left( \frac{P_1}{T_1} \right) A \cos \theta_B, \quad (17)$$

where  $P_1$  is the initial longitudinal polarization and  $T_1$  is the longitudinal relaxation constant. The factor  $A \cos \theta_B$  incorporates the asymmetry parameter  $A$  of the  $e^+$ -angular distribution and the tile coordinate  $\theta_B$  relative to the  $B$ -field axis. It determines the amplitude of the LF  $\mu\text{SR}$  signal in each tile pair (see Sec. II C).

To extract  $\tau_\mu$ , a 2-parameter fit using Eqn. 16 is performed varying both the muon lifetime  $\tau_\mu$  and the initial polarization  $P_1$ . The relaxation constant  $T_1$  is fixed at  $T_1 = 28 \mu\text{s}$  (see Sec. V B 3), a choice that influences the “best-fit” value for the polarization  $P_1$  but not  $\tau_\mu$ . The asymmetry parameter  $A$  in Eqn. 17 depends on the coordinates  $(\theta_B, \phi_B)$  of the tile pair. This occurs because positron absorption and scattering processes by intervening materials yield a geometry-dependent angular and energy positron distribution in tile pairs. Therefore tile-dependent values of  $A(\theta_B, \phi_B)$  obtained from a GEANT simulation of the experimental setup are used. The asymmetries range from +0.30 to +0.40.<sup>12</sup>

Note the tile coordinates  $(\theta_B, \phi_B)$  are calculated relative to the center of the muon stopping distribution not

<sup>11</sup> In the quartz production data the longitudinal polarization is  $P_1 \leq 0.01$  and longitudinal relaxation constant is  $T_1 = 28 \pm 8 \mu\text{s}$  and therefore the condition  $T_1/P_1 \gg \tau_\mu$  is fulfilled. For further details see Sec. V B.

<sup>12</sup> In practice the difference in  $\tau_\mu$  between using the GEANT calculated asymmetries  $A(\theta_B, \phi_B)$  and theoretical energy-integrated  $A = 1/3$  is 0.11 ppm.

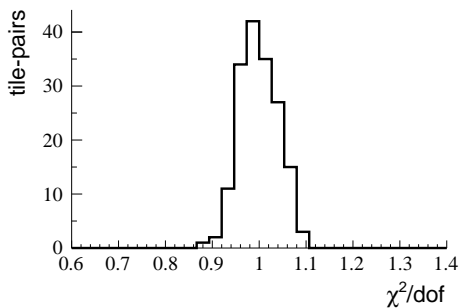


FIG. 18: The distribution of  $\chi^2/\text{dof}$  values from the 170 fits to the individual time histograms for the R07-A dataset. The fit function (Eqn. 14) incorporates the TF  $\mu\text{SR}$  signal.

the detector array. The position offsets ( $\delta x, \delta y, \delta z$ ) of the stopping distribution from the detector center are obtained from the measured distribution of the outgoing positrons in the tile array. The offsets are determined to a precision of  $\pm 2$  mm.

Figs. 17 and 18 show for dataset R07-A the fit to the angular distribution of the 170 effective lifetimes  $\tau_{\text{eff}}(\theta_B, \phi_B)$  and the results for the  $\chi^2/\text{dof}$  values from the 170 tile-pair time fits. The distribution of the  $\chi^2/\text{dof}$  values from the time fits has an average 1.0, which demonstrates that TF  $\mu\text{SR}$  effects are correctly handled. The fit of the  $\tau_{\text{eff}}$ -distribution has a  $\chi^2/\text{dof}$  of 201/168, which demonstrates the LF  $\mu\text{SR}$  effects are reasonably handled. The  $\chi^2$  of fits to decay time and  $\tau_{\text{eff}}$  distributions for other quartz datasets are of similar quality (see Table II).

Table II summarizes the parameters derived from the application of this method to the quartz datasets. There is good agreement between the  $\tau_{\mu}$ -values extracted from the six datasets.

Because the six datasets involve different magnet orientations and different detector positions, the fitted values of the initial longitudinal and transverse polarizations may differ.<sup>13</sup> The small values of  $P_1$  result from the perpendicular arrangement of the muon spin and the  $B$ -field while the small values of  $P_2$  results from the spin dephasing of the muon stops.

### B. Supplemental information on $\mu\text{SR}$ effects

In AK-3 the 3-parameter fit is successful because  $\mu\text{SR}$  signals are weak and cancel in sums of opposite tile pairs. In quartz the 5-parameter time distribution fits and 2-parameter  $\tau_{\text{eff}}$  distribution fit accounts for all observed TF/LF  $\mu\text{SR}$  distortions. We describe here supplemental information that further establishes that the  $\mu\text{SR}$  effects in AK-3 and quartz were handled correctly.

<sup>13</sup> In particular,  $P_1$  is very sensitive to the exact angle between the Halbach magnet field and the muon spin axis.

### 1. $\mu\text{SR}$ studies in AK-3

For decay times  $t > 100$  ns, no evidence for TF  $\mu\text{SR}$  is observed in AK-3. The absence of TF signals is expected as a consequence of the different axes and the varying frequencies of the spin rotation in the individual AK-3 magnetic domains.

A tiny TF  $\mu\text{SR}$  distortion, compatible with the fast relaxation of the transverse polarization of the last muon arrivals during the accumulation period, is seen at times  $t < 100$  ns. The signal is consistent with results from  $\mu\text{SR}$  studies on AK-3 by Morenzoni *et al.* [21] and Scheuermann *et al.* [42]. Both studies found evidence of spin relaxation with time constants of  $\sim 14$  ns and  $\sim 50$  ns, but no indications of longer timescales.

As shown in Fig. 19, a tiny variation of the fitted lifetime versus the detector angle  $\theta$  relative to the beam axis is observed. This effect is attributed to the slow relaxation of the longitudinal polarization  $P_1$ .

The longitudinal relaxation axis is approximately parallel to the beam axis while the AK-3 magnetization axis is oriented perpendicular to the beam axis. We believe this originates from the partial alignment of the AK-3 magnetic domains along the AK-3 magnetization axis. Consequently, while  $P_1$  accrues only small contributions from stops in domains oriented nearly perpendicular to the  $\mu$ -spin axis, it accrues much larger contributions from stops in domains oriented more parallel to the  $\mu$ -spin axis. The result is an ensemble-averaged longitudinal polarization that is roughly parallel to the beam axis.

The LF  $\mu\text{SR}$  effect on the fitted lifetime versus detector coordinate  $\theta$  is roughly 10 ppm. Supplemental data was acquired that enhanced  $P_1$ . The circular-cross section target, oriented at  $90^\circ$  to the beam axis, was replaced by an elliptical-cross section target, oriented at  $45^\circ$  to the beam axis. This increased the component of the AK-3 magnetization along the  $\mu$ -spin axis. The elliptical-target data shows a four-fold increase in lifetime variation with detector coordinate  $\theta$ . This is qualitatively consistent with the expected increase in the polarization  $P_1$ .<sup>14</sup> It supports our argument that the  $\theta$ -dependence of the fitted lifetime originates from a longitudinal relaxation in the AK-3 target, and therefore will cancel in sums of opposite tile pairs.

<sup>14</sup> A quantitative prediction of the longitudinal polarization increase for the elliptical target requires a detailed knowledge of the domain orientations. However, the observed four-fold increase in the  $\theta$ -variation of the fitted lifetime is consistent with a simple model of populations of fully aligned domains and randomly aligned domains that reproduces the ratio between the known AK-3 remnant and saturation fields [19].

TABLE II: Results of the fitting method for the six quartz datasets. The entries for the transverse polarization  $P_2$  are weighted averages obtained from tile-pairs having large TF  $\mu$ SR signals. The entries for the longitudinal polarization  $P_1$  are individual values obtained from effective lifetime fits. The parameter  $T_2 = 4.7 \mu\text{s}$  is fixed from fits to time histograms with large TF  $\mu$ SR signals and the parameter  $T_1 = 28 \mu\text{s}$  is fixed from fits to supplemental data with amplified LF  $\mu$ SR signals. The offsets  $(\delta x, \delta y, \delta z)$  are fixed from the geometrical distribution of hits over the positron detector.

parameter	data set					
	R07-A	R07-B	R07-C	R07-D	R07-E	R07-F
$P_2 \times 1000$	$2.54 \pm 0.02$	$2.45 \pm 0.02$	$2.35 \pm 0.05$	$2.51 \pm 0.07$	$2.28 \pm 0.05$	$2.54 \pm 0.06$
$\omega$ (Rad/ $\mu\text{s}$ )	$11.4440 \pm 0.0061$	$11.5342 \pm 0.0066$	$11.570 \pm 0.016$	$11.489 \pm 0.019$	$11.579 \pm 0.016$	$11.498 \pm 0.018$
$P_1 \times 1000$	$1.3 \pm 0.2$	$1.6 \pm 0.2$	$1.3 \pm 0.4$	$1.2 \pm 0.7$	$0.7 \pm 0.5$	$1.5 \pm 0.6$
$\tau_\mu$ (ps)	$2196981.93 \pm 5.86$	$2196980.94 \pm 5.51$	$2196975.43 \pm 15.11$	$2196967.24 \pm 22.79$	$2196985.33 \pm 15.66$	$2196991.11 \pm 20.40$
$\chi^2/\text{dof}$	200.9/168	174.2/168	154.9/168	153.0/168	167.1/168	172.1/168
beam $x$ (cm)	-0.3	-0.4	-1.4	-0.7	-0.9	-1.0
beam $y$ (cm)	-0.3	0.1	0.9	0.75	-0.1	0.6
beam $z$ (cm)	0.07	0.06	0.06	0.06	0.06	-0.1

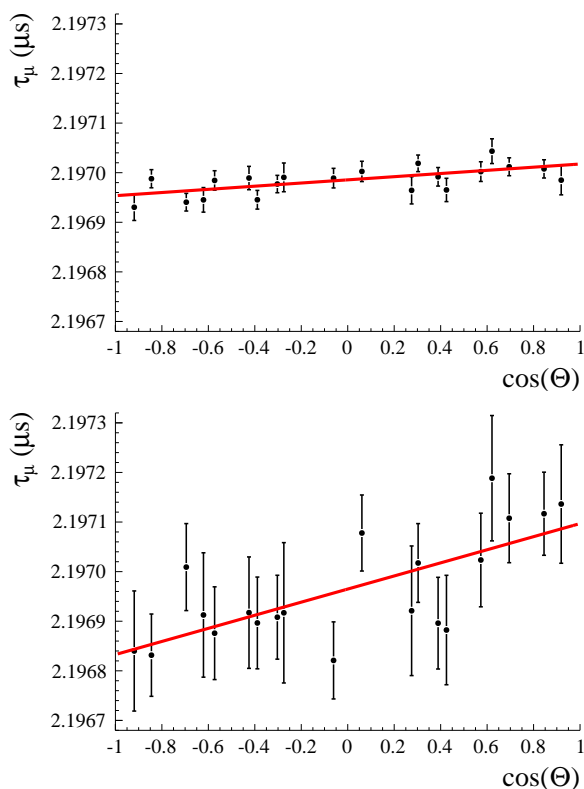


FIG. 19: Plots of the fitted lifetimes from the individual time histograms grouped by the detector angle  $\theta$  relative to the beam axis. The upper panel represents the AK-3 production data with the magnetization axis at 90 degrees to the beam axis. The lower panel represents the AK-3 supplemental data with the magnetization axis at 45 degrees to the beam axis. The four-fold increase in the  $\theta$ -dependence of the fitted lifetime in the lower plot reflects the increase in the longitudinal polarization for the 45 degree dataset. Note the vertical scales on the two plots are the same.

## 2. Transverse field $\mu$ SR studies in quartz

Figure 20 (upper panel) shows the ratio

$$R_{UD}(t) = \frac{N_U(t) - N_D(t)}{N_U(t) + N_D(t)} \quad (18)$$

involving the normalized time distributions of the coincidence hits  $N_{U/D}(t)$  in the upstream/downstream hemispheres of the positron detector.<sup>15</sup> This diagnostic is sensitive to time-dependent differences between upstream/downstream hits and clearly shows a TF precession signal with a frequency  $\omega \sim 11 \mu\text{s}^{-1}$  and a time constant  $T_2 \sim 5 \mu\text{s}$ . The value of  $\omega$  agrees with the expected value for a diamagnetic  $\mu^+$  population in the 130 G Halbach magnet field.

The relative amplitude of the TF  $\mu$ SR signal in the production data is only  $\sim 10^{-3}$ . To further study the TF  $\mu$ SR signal, a supplemental dataset was acquired by shortening the accumulation period from  $T_A = 5.0$  to  $0.15 \mu\text{s}$  and thereby reducing roughly 20-fold the spin dephasing during muon accumulation. As depicted in Fig. 20 (lower panel), the ratio  $R_{UD}(t)$  obtained with  $T_A = 0.15 \mu\text{s}$  shows a large TF signal consistent with a twenty-fold enhancement of the production data signal. Fits using Eqn. 14 to the time histograms derived from the  $T_A = 0.15 \mu\text{s}$  dataset indicate a quartz diamagnetic  $\mu^+$  population of roughly 6-7%, in good agreement with published work [24, 25].

<sup>15</sup> A subtraction of the time-independent background and a normalization of the summed histogram contents, is performed before deriving the ratio  $R_{UD}(t)$  from the  $N_{U/D}(t)$  spectra.

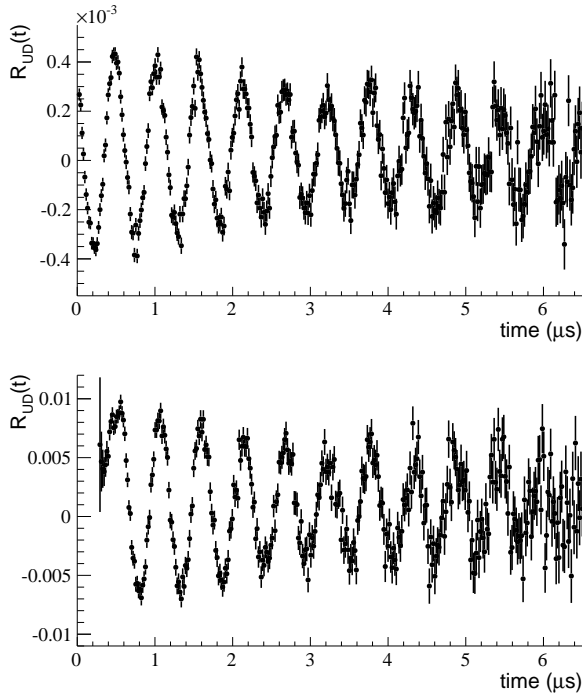


FIG. 20: Ratio  $R_{UD}(t)$  of the normalized difference between the time distributions in the upstream/downstream hemispheres of the positron detector. The upper panel corresponds to production data with an accumulation period  $T_A = 5.0 \mu\text{s}$  and the lower panel corresponds to supplemental data with a shortened accumulation period  $T_A = 0.15 \mu\text{s}$  (note the different scales of the vertical axes). The plots highlight the contribution of the TF  $\mu\text{SR}$  signal in the quartz data.

### 3. Longitudinal field $\mu\text{SR}$ studies in quartz

The two ratios

$$\begin{aligned} R_L(t) &= N_L(t)/(N_L(t) + N_R(t)) \\ R_R(t) &= N_R(t)/(N_L(t) + N_R(t)) \end{aligned} \quad (19)$$

are plotted in Fig. 21.  $N_L(t)$  and  $N_R(t)$  correspond to the normalized time distributions of the coincidence hits in the beam-left and beam-right hemispheres of the positron detector, respectively.<sup>16</sup> These rates are sensitive to time-dependent differences between beam-left and right hits and suggest a gradual decrease (increase) in  $R_L(t)$  ( $R_R(t)$ ) consistent with a long-timescale relaxation of the muon longitudinal polarization along the  $B$ -field axis. The time constant  $T_1$  of the relaxation is much longer than the  $\mu^+$  lifetime.

<sup>16</sup> A (i) subtraction of the time-independent background and (ii) normalization of the summed histogram contents is performed before deriving the ratios  $R_{L/R}(t)$  from the  $N_{L/R}(t)$  spectra.

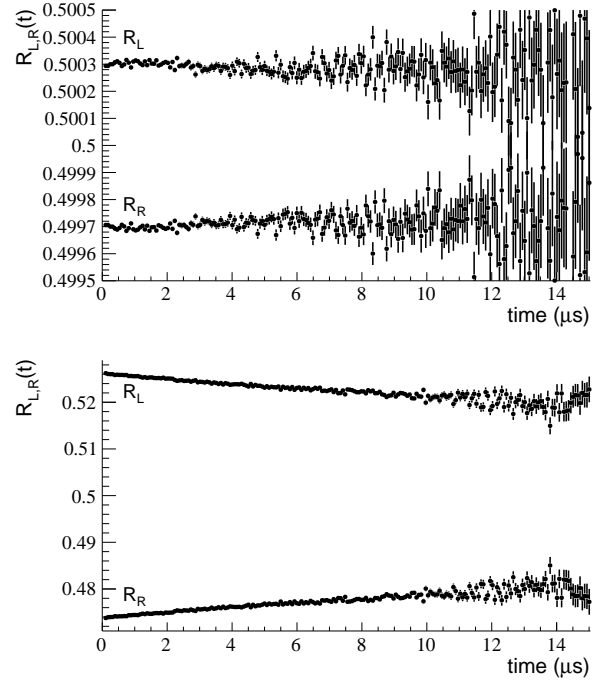


FIG. 21: Ratio of hit time distributions from the beam-left hemisphere ( $R_L(t)$ ) and the beam-right hemisphere ( $R_R(t)$ ) to the detector sum. The upper panel corresponds to production data with a longitudinal polarization  $P_1 \sim 0.01$  and the lower panel corresponds to supplemental data with a longitudinal polarization  $P_1 \sim 0.25$ . The gradual slopes in  $R_{L/R}(t)$  are the effect of the LF  $\mu\text{SR}$  in the quartz data.

The relative amplitude of the LF  $\mu\text{SR}$  signal in the production data is only  $10^{-4}$ . Supplemental datasets were acquired with enhanced LF effects by re-orientating the Halbach magnet from a perpendicular alignment to the  $\mu^+$  spin axis ( $P_1 \leq 0.01$ ) to non-perpendicular alignments ( $P_1 \sim 0.05 - 0.25$ ).

Fig. 21 shows the ratios  $R_{L/R}(t)$  for the  $P_1 \sim 0.25$  dataset and clearly indicates a gradual decrease (increase) in  $R_L(t)$  ( $R_R(t)$ ) consistent with a roughly twenty-fold enhancement of the LF  $\mu\text{SR}$  signal. Fits of Eqn. 16 to the time histogram from the  $P_1 = 0.05$  to 0.25 datasets give a relaxation constant  $T_1 = 28 \pm 8 \mu\text{s}$ .

### C. Consistency checks

A number of checks are performed on the overall consistency of the lifetime results. They include comparisons of fit results for different time ranges, run groups, detector positions and  $B$ -field orientations.

Fig. 22 shows the fitted lifetime versus the fit start time from  $t_{start} = 0.1$  to  $5.0 \mu\text{s}$  for the AK-3 and quartz data. The points indicate the lifetime results from individual fits and the solid curves their permissible deviations ( $1\sigma$ )

from the benchmark fit with a start time  $t_{start} = 0.2 \mu\text{s}$ . The deviations account for the correlations between the individual fits and the benchmark fit. No evidence is seen for either a start-time dependence or a stop-time dependence of the lifetime. This builds confidence in the handling of known time-dependent effects including  $\mu\text{SR}$  signals, positron pileup and gain changes, as well as the absence of any unidentified time-dependent distortions.

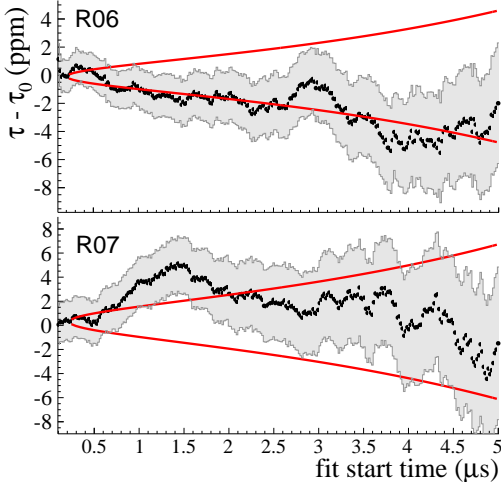


FIG. 22: Muon lifetime versus fit start-time for the AK-3 data (top) and the quartz data (bottom). The data points and gray band indicate the lifetime results and corresponding uncertainties from individual fits. The solid envelopes indicate the permissible statistical deviations ( $1\sigma$ ) from the benchmark fits with a start-time  $t_{start} = 0.2 \mu\text{s}$ . The  $1\sigma$  deviations are calculated with appropriate accounting for dataset correlations between different fit ranges.

Fig. 23 shows  $(\tau_i - \tau_\mu)/\sigma_i$ , the normalized deviations of lifetime values  $\tau_i$  for the individual runs from the benchmark result  $\tau_\mu$ . The figure indicates the normalized deviations form a Gaussian distribution of mean zero and

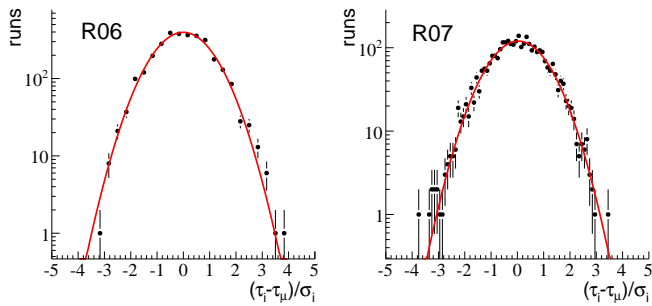


FIG. 23: The distribution  $(\tau_i - \tau_\mu)/\sigma_i$  of the normalized deviations of the fitted lifetimes  $\tau_i$  from the individual runs from the final result  $\tau_\mu$ . The data points are the run-by-run results and the solid curve is a least squares fit to a Gaussian distribution. The left panel is the AK-3 dataset and the right panel is the quartz dataset.

standard deviation 1.0, *i.e.*, consistent with purely statistical variations. These results for individual run variations, and similar results for run group variations, demonstrate the absence of effects on  $\tau_\mu$  from long-timescale changes in gains, pedestals and thresholds.

Recall in AK-3 (quartz) tiny variations of the fitted lifetime with the coordinate  $\theta$  ( $\theta_B$ ) are observed. These effects are attributed to the slow relaxation of the longitudinal polarization and are expected to cancel out in opposite-pair sums. However, such  $\mu\text{SR}$  cancellation grows increasingly imperfect for a source that is displaced from the center of the detector.

The  $\theta(\theta_B)$ -distribution of the lifetime values obtained by fitting summed time histograms of geometrically-opposite tile-pairs in AK-3 (quartz) are plotted in Fig. 24. Neither show any evidence for a systematic  $\theta(\theta_B)$ -dependence of the fitted lifetimes (as could originate from imperfect cancellation of  $\mu\text{SR}$  distortions from upstream stops).

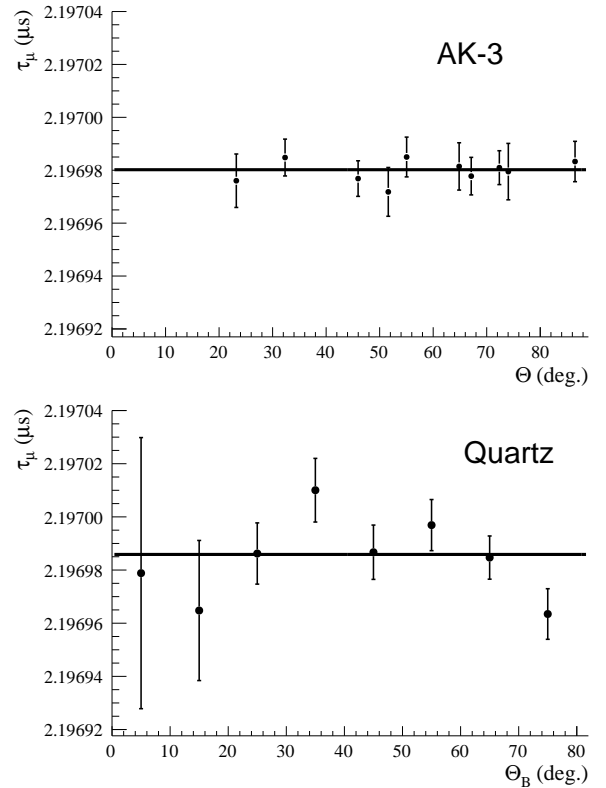


FIG. 24: The upper panel shows the lifetime results from opposite tile-pair sums grouped by detector coordinate  $\theta$  for the entire AK-3 dataset. The lower panel shows the lifetime results from opposite tile-pair sums grouped by detector coordinate  $\theta_B$  for the entire quartz dataset. The plots demonstrate the cancellation of  $\mu\text{SR}$  distortions from target stops in opposite tile pairs.

A number of datasets were accumulated with different magnetic field orientations and different positron detector offsets ( $\delta x, \delta y, \delta z$ ). The agreement between lifetime

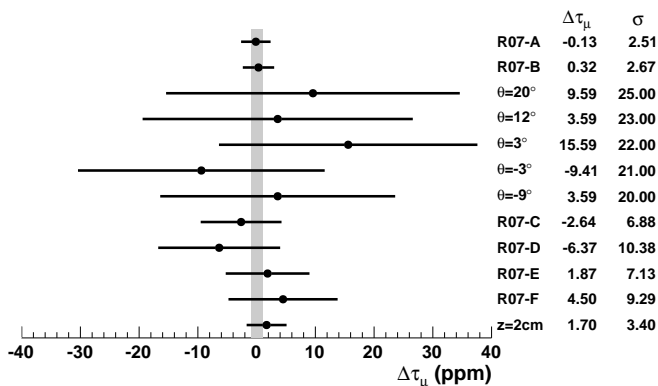


FIG. 25: Fitted lifetime for quartz datasets with different magnetic field orientations and positron detector offsets. Entries R07-A and R07-B correspond to the quartz production data with the  $B$ -field orientation to the beam-left and beam-right, respectively. Entries R07-C through R07-F correspond to quartz production data with different detector positions and entries  $\theta = -9.0^\circ$  through  $\theta = 20.0^\circ$  correspond to quartz systematics data with different magnet tilt angles. The different detector positions and magnet angles change the magnitudes and axes of the LF/TF polarizations and their corresponding  $\mu$ SR signals.

results for different magnet and detector configurations is an important requirement for the overall handling of the  $\mu$ SR distortions.

We conducted the most exhaustive studies on the larger  $\mu$ SR signals from the quartz target. The quartz studies spanned a wide range of precession axes (from horizontal to vertical) and longitudinal polarizations (from  $\sim 0.001$  to  $\sim 0.25$ ). The specific datasets were

- (i) Production quartz data accumulated with the Halbach magnet  $B$  field oriented to the beam-left and the beam-right. This change reverses the precession direction.
- (ii) Supplemental quartz data accumulated with the Halbach magnet  $B$ -field tilted at pitch angles up to  $40^\circ$  from the vertical. This changes both the axis of the TF precession and the magnitude of the LF relaxation.
- (iii) Both quartz production and supplemental data accumulated with different offsets ( $\delta x, \delta y, \delta z$ ) between the detector center and the stopping distribution (the changes in offset were  $\leq 2$  cm). This changes the magnitude and direction of the Halbach  $B$ -field at the stopping location and therefore the frequency of the TF precession and the amplitude of the LF relaxation.

Fig. 25 summarizes the lifetime values derived from the left/right  $B$ -field orientations, vertical/tilted  $B$ -field orientations and different target-detector offsets. The good

agreement between lifetime values obtained with different TF/LF  $\mu$ SR signals verifies that muon spin rotation in quartz was handled correctly.

Finally, we remark that the AK-3 production datasets were also accumulated with the target magnetization oriented to the beam-left and the beam-right.

## D. Systematics studies

This section addresses four classes of systematic uncertainties. One class of effect is associated with corrections for pulse pileup and gain changes in the histogram construction and another class is associated with  $\mu$ SR effects in the histogram fits. A third class is related to possible time-dependent backgrounds such as muon stops in the upstream beam pipe and a time-varying extinction of the muon beam. A final class is the overall stability of the time measurement.

### 1. Artificial deadtime correction

A correction is applied for the lost hits during the artificial deadtime (see Sec. IV C 1). The pileup correction is performed for artificial deadtimes (ADTs) of 5 to 68 c.t. (11 to 151 ns). By increasing the ADT, one decreases the trigger-hit histogram contents and increases the shadow-hit histogram contents. Assuming the procedure correctly accounts for digital pileup, the lifetime derived by summing trigger hit and shadow-hit histograms is independent of the applied ADT.

Fig. 26 shows  $\tau_\mu$  versus ADT both before and after the pileup correction for the R07 dataset. Before the correction, the lifetime increases by 10.5 ppm/ns (R06) and 10.6 ppm/ns (R07), while after the correction, the lifetime increases by 0.008 ppm/ns (R06) and 0.007 ppm/ns (R07), a roughly 1000-fold reduction in the ADT-dependence of the lifetime  $\tau_\mu$ .

A “perfect” correction of pileup would yield an ADT-independent lifetime. The tiny residual slope in  $\tau_\mu$  versus ADT after correcting for pileup thereby implies the procedure is slightly under-estimating the artificial deadtime effects at the level of about  $10^{-3}$ . One possible explanation is either the omission of a small, high-order, pileup term or the mis-accounting for a larger, known, pileup term. However, as discussed in Sec. IV C 1, the procedure for accounting for digital pileup was verified by Monte Carlo simulation and indicated no evidence of any omitted terms or mis-accounted terms at the  $10^{-3}$  level.

Another possible explanation is a non-statistical variation of the muon stops in the accumulation periods. Non-statistical variations lead to a pileup under-correction for “high rate” fills and a pileup over-correction for “low

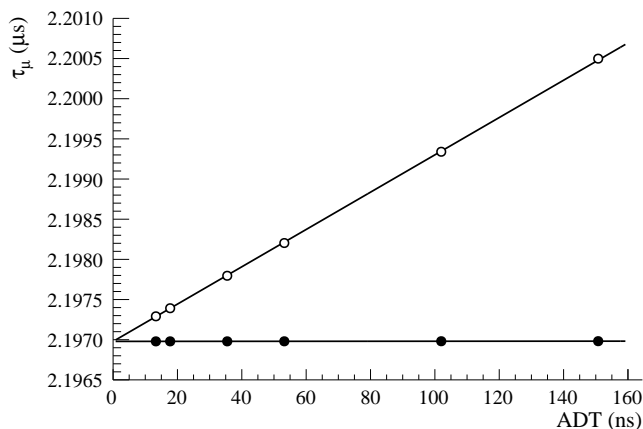


FIG. 26: Plot of  $\tau_\mu$  versus ADT before the pileup correction (open circles) and after the pileup correction (filled circles). The statistical uncertainties associated with the pileup correction are substantially smaller than the statistical uncertainty on the muon lifetime and not visible on this scale. The solid lines through data points are only to guide the eye.

rate” fills that does not cancel out exactly.<sup>17</sup> Although sources of non-statistical variations are known—*e.g.* ion source fluctuations and production target rotation—their effects on muon stops are insufficient to explain the slope in  $\tau_\mu$  versus ADT.

Although no conclusive explanation for the ADT-dependence of the fitted lifetime is identified, the observed variation of  $\tau_\mu$  versus ADT is clearly linear. Therefore the lifetimes derived from ADT = 6 c.t. (13.3 ns) fits are corrected by linear extrapolations to zero deadtime. The extrapolation uses the slope obtained from a straight-line fit to  $\tau_\mu$  versus ADT from 5 to 68 c.t. (11-151 ns). The extrapolation yields a decrease in  $\tau_\mu$  of 0.11 ppm for the AK-3 data and 0.10 ppm for the quartz data. A conservative systematic uncertainty of  $\pm 0.2$  ppm is assigned to the digital pileup correction procedure.

## 2. Below-threshold pulses

In the absence of pileup, below-threshold pulses cannot generate hits. Two pileup effects involving below-threshold pulses are important:

- (i) “Pile-on” involves the pileup of two below-threshold pulses. If the pulses overlap, the below-threshold pulses can produce a single above-threshold pulse. Pile-on is a rate dependent increase in hits that distorts the time distributions.

Because unaccounted pile-on adds hits at high rates (early times), it decreases the fitted  $\tau_\mu$ .

- (ii) “Pile-down” involves the pileup of one below-threshold pulse and one above-threshold pulse. If the pulses do not overlap, the below-threshold pulse can raise the pedestal and lower the amplitude of the fitted above-threshold pulse. Pile-down is a rate dependent decrease in hits that distorts the time distributions. Because unaccounted pile-down removes hits at high rates (early times), it increases the fitted  $\tau_\mu$ .

The effects of pile-on in promoting below-threshold pulses, and pile-down in demoting above-threshold pulses, are not ADT-dependent and are not corrected by the shadow window technique. The two effects cause opposite shifts in  $\tau_\mu$ . For a pulse fitting procedure that is linear in the amplitude  $A$  and the pedestal  $P$  and equally weights all ADC samples, the effects exactly cancel. However, the exact cancellation is defeated if below-threshold pulses are first identified in the pulse fitting and then dismissed by the amplitude cut.

A complete evaluation of pile-on and pile-down requires the measurement of the below-threshold amplitude distribution. To avoid biases from the hardware threshold of the waveform digitizers, the distribution was measured by acquiring data using an extended, 64-sample data block; the region of samples from 32 to 64 being used to obtain an unbiased amplitude distribution. A relatively large number of pulses having amplitudes  $< 25$  ADC counts is found that carry no time dependence. A relatively small number of pulses having amplitudes 25-35 ADC counts is found that do carry the muon lifetime.

Using the measured amplitude distributions, the combined effects of pile-on and pile-down on  $\tau_\mu$  are estimated by Monte Carlo simulation to be less than 0.2 ppm. Importantly, the combined effects of pile-on and pile-down are manifest in the time dependence of the amplitude spectrum during the measurement period, and therefore are compensated by the application of the gain correction to the time histograms (see Sec. IV C 2).

## 3. Time pick-off stability

Pileup can result in the loss of valid hits or the addition of extra hits. Pileup can additionally “pull” the time determination of tile pulses through effects including the absorption of a small, overlapping pulse into the trigger pulse fit or the interference of a large, preceding pulse with the trigger pulse fit. Such distortions of the time “pick-off” are rate-dependent and therefore can distort  $\tau_\mu$ .

The determination of the time pick-off stability is conducted using the 24 tiles instrumented with the optical fibers from the pulsed-laser system. Approximately 400 laser runs were accumulated in each production run. The

<sup>17</sup> The effects do not cancel as the number of under-corrected hits in high-rate fills exceeds the number of over-corrected hits in low-rate fills.



time difference  $\delta t(t)$  between laser pulses in the scintillator tiles and the reference PMT is sensitive to any rate-dependent shifts in the time pick-off from the tile pulses.<sup>18</sup>

To determine the time difference  $\delta t(t)$  versus measurement time  $t$ , a series of time difference histograms are accumulated corresponding to sequential 2.5  $\mu\text{s}$ -wide time windows on the laser pulse time during the measurement period. These histograms are then fit to a Gaussian distribution with the centroids determining  $\delta t(t)$ . The fitted slopes of  $\delta t(t)$  versus  $t$  for all tiles are consistent with zero. By combining results from all tiles, the average time pick-off was found to change by less than 0.25 ps over the measurement period. The limit implies a negligible distortion of  $\tau_\mu$ .

#### 4. Gain variations

For the normal amplitude threshold  $A_{thr}$ , the lifetime shifts resulting from gain variations are  $0.50 \pm 0.25$  ppm (R06) and  $0.53 \pm 0.25$  ppm (R07). The uncertainties of 0.25 ppm are conservative and based on variations between alternative procedures for making the gain corrections (see Sec. IV C 2). The separate shifts for pairs instrumented with the Electron Tube PMTs (22 tile pairs) and Photonis PMTs (148 tile pairs) are  $+5.0$  and  $-0.2$  ppm for the R06 dataset and  $+5.3$  and  $-0.1$  ppm for the R07 dataset. The separate values of  $\tau_\mu$  obtained from Electron Tube and Photonis PMTs—after the appropriate correction for the gain variation—are in reasonable agreement for the two datasets.

To test the procedure for correcting for gain variations, time spectra having amplitude thresholds  $A_{thr}+20$ ,  $+30$  and  $+40$  ADC units were obtained. Increasing the threshold increases the  $\tau_\mu$  sensitivity to gain changes due to a higher count fraction in the threshold amplitude bin (see Eqn. 11). The  $A_{thr} + 20$ ,  $+30$  and  $+40$  settings increase the lifetime distortions from gain variations by factors of roughly 10, 30 and 50, respectively. A small error in the gain correction procedure at the normal amplitude threshold thus implies a large error in the gain correction procedure at the higher amplitude thresholds. Lifetimes obtained from a 10% fraction of the R06/R07 datasets with the  $A_{thr} + 20$ ,  $+30$  and  $+40$  settings—with 50-fold differences in gain corrections—are in reasonable agreement.

#### 5. AK-3 $\mu\text{SR}$

The application of the fitting method to the AK-3 data relies on geometrical cancellation of  $\mu\text{SR}$  effects, in par-

ticular the  $\sim 10$  ppm variation of the fitted lifetime with the tile-pair angle  $\theta$  about the beam axis. The cancellation is not exact owing to differences in the detector acceptances (for example, variations in tile efficiencies, electron absorption in intervening materials, and the mis-centering of the stopping distribution). An acceptance variation between opposite tile pairs of several percent is estimated from the measured variations of the positron rates in the scintillator tiles. By combining the observed  $\theta$ -dependence of the lifetime  $\tau_\mu$  with the estimated variation of the opposite tile-pair acceptances, a 0.1 ppm systematic uncertainty from AK-3  $\mu\text{SR}$  effects is derived.

#### 6. Quartz $\mu\text{SR}$

As described in Sec. V A 2, the handling of  $\mu\text{SR}$  effects in quartz requires specifying the beam-detector offset,  $B$ -field axis and several  $\mu\text{SR}$  parameters.

In fitting the time histograms of tile-pairs, the precession frequency  $\omega$  and relaxation constant  $T_2$  are fixed to their “best fit” values (see Fig. 27). The change in  $\tau_\mu$  when  $\omega$  and  $T_2$  are varied by one standard deviation from their “best-fit” values is adopted as the associated systematic uncertainties. The procedure yields uncertainties in  $\tau_\mu$  of 0.003 ppm from fixing  $\omega$  and 0.02 ppm from fixing  $T_2$ .

The fit to the angular distribution of the effective lifetimes requires the determination of the tile coordinates  $(\theta_B, \phi_B)$  relative to the  $B$ -field axis. A  $\pm 2^\circ$  uncertainty is assigned to the knowledge of the  $B$ -field axis based on the uncertainties in the mechanical alignment of the Halbach magnet and the  $B$ -field non-uniformities at the target location.<sup>19</sup> The uncertainty in  $\tau_\mu$  is obtained by correspondingly varying the  $B$ -field axis in the fit procedure for the effective lifetimes (Sec. V A 2). The approach yields an associated uncertainty of 0.004 ppm in  $\tau_\mu$ .

Also required in the fitting procedure to the effective lifetimes are the offsets  $(\delta x, \delta y, \delta z)$  between the centers of the positron detector and the stopping distribution. These offsets are determined from measured differences between positron rates in opposite tile-pairs. A  $\pm 2$  mm uncertainty is assigned to the determination of the offsets  $(\delta x, \delta y, \delta z)$ , based on the estimated variations in the tile-pair detection efficiencies. The corresponding uncertainty in  $\tau_\mu$  is obtained by varying each offset by  $\pm 2$  mm in the fit procedure to the effective lifetimes. The approach yields an associated uncertainty of 0.19 ppm in  $\tau_\mu$ . The dominant contribution originates from the offset  $\delta x$  along the direction of the longitudinal relaxation.

Finally, an uncertainty in  $\tau_\mu$  is associated with the positron asymmetries  $A(\theta_B, \phi_B)$  required in the effective lifetime fit procedure. This uncertainty is based

<sup>18</sup> The scintillator tile rate falls during the measurement period while the reference PMT rate is constant during the measurement period.

<sup>19</sup> The estimate of a  $\pm 2^\circ$  uncertainty in the  $B$ -field axis is consistent with the observed longitudinal polarizations in the quartz production data.

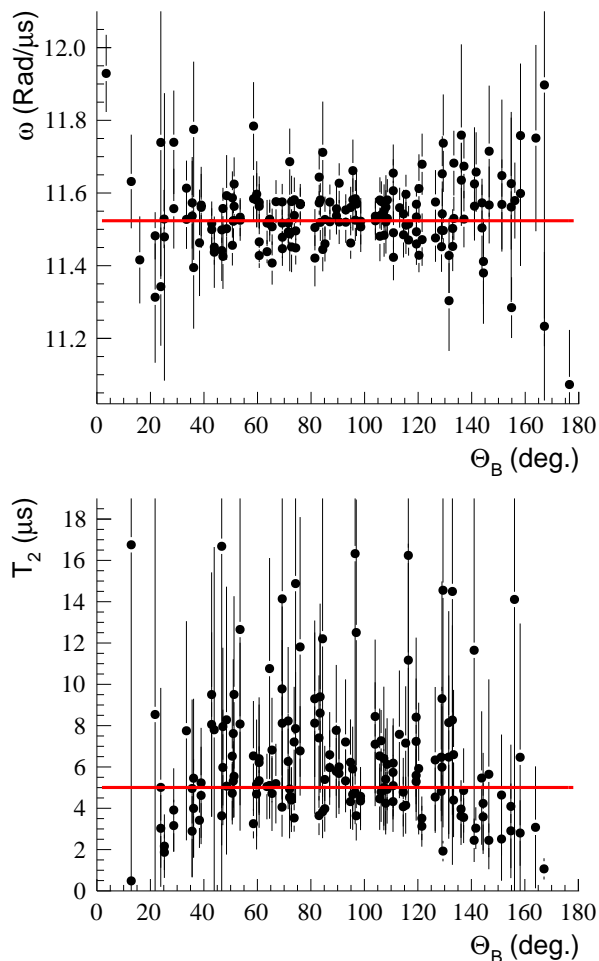


FIG. 27: Examples of precession frequency  $\omega$  (upper panel) and relaxation constant  $T_2$  (lower panel) versus tile coordinate  $\theta_B$  obtained from 7-parameter fits using Eqn. 14. The solid horizontal lines indicate the fixed “best fit” values of  $\omega$  and  $T_2$  that are used in the fits of the tile-dependent effective lifetimes.

on the difference between  $\tau_\mu$  obtained with the tile-dependent, GEANT-calculated asymmetries and the tile-independent, energy-integrated theoretical asymmetry  $A = 1/3$ . The approach yields an associated uncertainty of 0.05 ppm in  $\tau_\mu$ .

Table III summarizes the various contributions to the systematic uncertainty in  $\tau_\mu$  associated with the fitting procedure for the quartz  $\mu$ SR effects. The total uncertainty in  $\tau_\mu$  from quartz  $\mu$ SR effects is 0.2 ppm.

### 7. Upstream muon stops

A small fraction of muons stop on the inner walls of the beampipe upstream of the target disk. These stops include both incoming muons in the beam halo and back-scattered muons from the stopping target. Both tar-

TABLE III: Compilation of the contributions to the systematic uncertainty in the lifetime  $\tau_\mu$  from the fitting procedure for the  $\mu$ SR effects in the quartz data.

parameter	$\delta\tau_\mu$ (ppm)
$\omega$	0.003
$T_2$	0.021
$(\theta_B, \phi_B)$	0.004
$\delta x$	0.19
$\delta y$	0.001
$\delta z$	0.001
$A$	0.05
Total uncertainty	0.20

get disks were sufficiently thick to eliminate downstream stops.

The concern with upstream stops is potential shifts of  $\tau_\mu$  arising from  $\mu$ SR. Unlike target stops, where  $\mu$ SR signals cancel in opposite tile-pair sums, for upstream stops, the  $\mu$ SR signals do not cancel out. Therefore the presence of  $\mu$ SR signals from upstream stops could distort  $\tau_\mu$ .

Recall that following the downstream beamline elements, the vacuum-pipe diameter was reduced from 35.5 cm to 20.2 cm at a location 52 cm upstream of the stopping target. To minimize any  $\mu$ SR effects, a 67 cm long section of the pipe immediately upstream of the stopping target was lined with 0.3 mm-thick AK-3 foil. To maximize dephasing, the AK-3 magnetization was oriented perpendicular to the beam axis.

Several measurements were conducted to estimate the effects of upstream stops. Two regions of beampipe are particularly worrisome; (i) the location of the beampipe constriction and (ii) the section of the reduced-diameter beampipe.

To estimate the stopping fraction in the annular face of the pipe constriction, a  $2 \times 3$  cm<sup>2</sup> cross section, 3-mm thick, plastic scintillator was mounted on a vacuum feed-through in the beampipe region that was immediately upstream of the pipe constriction. The setup determined the radial dependence of the muon rate along horizontal, vertical and 45°-angled axes perpendicular to the beam direction. The measurements yielded an estimate of  $(0.5 \pm 0.1)\%$  for the stopping fraction in the pipe constriction.

To estimate the stopping fraction in the 20.2 cm diameter beam pipe, a plastic scintillator telescope was used to detect the outgoing positrons from beampipe stops. The telescope consists of two pairs of separated scintillator tiles that viewed a  $\sim 10$  cm diameter region of beampipe. The measurement yielded a stopping fraction of  $(0.10 \pm 0.05)\%$  in the 20.2 cm diameter beampipe.

The combined results of measurements (i) and (ii) indicate less than a 1.0% upstream stopping fraction. To determine the effects of upstream stops, a dedicated dataset of upstream stops was collected. The dataset comprised  $\sim 2 \times 10^{10}$  stops in magnetized AK-3 at twelve upstream locations of 5 to 80 cm from the detector center. The

lifetimes derived from this upstream stop data and the production data are in good agreement. When the upstream stop data and the production data are added in proportions of 1:100 the lifetime decreases by 0.1 ppm.

### 8. Beam extinction stability

A time-dependent beam extinction ( $\epsilon \sim 900$ ) will cause a time-dependent positron background. A variation of extinction can arise from a systematic change in the kicker voltage during the measurement period.

A limit on lifetime distortions from voltage instabilities is derived by combining: (i) a measurement of the kicker voltage  $V(t)$  over the measurement period, and (ii) a measurement of the beam extinction  $\epsilon(V)$  versus the kicker voltage, with (iii) a simulation of the effects of a time-dependent background on the lifetime determination.

The kicker voltage was measured with a high voltage probe connected to the kicker deflector plates. The probe was read out using a digital oscilloscope and the average voltage  $V(t)$  from many kicker cycles was fit to determine a limit on the voltage drift during the measurement period. Data were obtained on several occasions during both production runs and yield limits of  $\Delta V < 300$  mV (R06) and  $\Delta V < 150$  mV (R07).<sup>20</sup>

The variation in beam extinction with kicker voltage  $\Delta\epsilon/\Delta V$  was measured during both production runs using the beam monitor. Over the kicker voltage range 23.5-25.0 kV the extinction increased linearly with increased voltage. Combining the limits on  $\Delta V$  with the determinations of  $\Delta\epsilon/\Delta V$ , the limits on changes in beam extinction from voltage instabilities of  $\Delta\epsilon < 0.20$  (R06) and  $\Delta\epsilon < 0.06$  (R07) are obtained.

A simulation is used to estimate the effect of an extinction variation  $\Delta\epsilon$  on the fitted lifetime  $\tau_\mu$ . First, a time distribution is generated, consisting of an exponential decay curve with a time-dependent background due to extinction variation. Then, the resulting distribution is fit to an exponential decay curve with a time-independent background. The difference  $\Delta\tau_\mu$  between the simulated lifetime and the fitted lifetime thereby determines the distortion of the lifetime originating from an unaccounted variation of the beam extinction. The procedure yields upper limits of 0.20 ppm (R06) and 0.07 ppm (R07) on the lifetime distortions from the kicker voltage drifts.

These limits are 20-40 times smaller than the limit quoted in our 2004 commissioning measurement. The improvements in limits were achieved through better suppression of voltage drifts, better measurements of voltage stabilities, and increased beam extinction.

### 9. Master clock stability

Finally, the master clock output was compared at several frequencies to a calibrated rubidium frequency standard. The comparisons were made at the beginning and the end of each running period. The observed deviations were less than 0.03 ppm over the duration of the experiment. A systematic uncertainty of 0.03 ppm on  $\tau_\mu$  is assigned to the time calibration of the master clock.

## VI. RESULTS

### A. Summary of uncertainties

Table IV summarizes the statistical and systematic uncertainties that contribute to the muon lifetime measurements in the R06 and R07 running periods. The uncertainties associated with  $\mu$ SR effects and kicker instabilities are considered to be independent contributions to the R06 and R07 systematics. The larger  $\mu$ SR uncertainty in R07 data-taking reflects the larger  $\mu$ SR distortions in the quartz data and the smaller kicker uncertainty in R07 data-taking reflects the improved limits on voltage instabilities.

By comparison, the uncertainties associated with pulse pileup, gain variations, upstream stops, time pick-off stability and clock calibration are considered to be common contributions to the R06/R07 running periods. In each case the same methods are used to obtain estimates of systematic uncertainties.

TABLE IV: Sources of systematic uncertainties on the muon lifetime measurements in the R06/R07 running periods. The uncertainties listed in single-column format are common uncertainties and those listed in two-column format are uncorrelated uncertainties. The last two rows are the combined systematic uncertainties and the overall statistical uncertainties for the R06/R07 datasets.

Uncertainty	R06 (ppm)	R07 (ppm)
Kicker stability	0.20	0.07
$\mu$ SR distortions	0.10	0.20
Pulse pileup		0.20
Gain variations		0.25
Upstream stops		0.10
Timing pick-off stability		0.12
Master clock calibration		0.03
Combined systematic uncertainty	0.42	0.42
Statistical uncertainty	1.14	1.68

### B. Results for muon lifetime, $\tau_\mu$

The individual results for the muon lifetime from the fits to the R06 (AK-3) dataset and the R07 (quartz)

<sup>20</sup> The “worst-case” voltage drift is obtained by examining a variety of fits (*e.g.* linear, exponential) to the kicker voltage during the measurement period. The values quoted for  $\Delta V$  are obtained from a linear fit.

dataset, after the  $-0.11$  ppm (R06) and  $-0.10$  ppm (R07) adjustments for the ADT = 0 extrapolation, are

$$\tau_\mu(\text{R06}) = 2\,196\,979.9 \pm 2.5(\text{stat}) \pm 0.9(\text{syst}) \text{ ps} \quad (20)$$

and

$$\tau_\mu(\text{R07}) = 2\,196\,981.2 \pm 3.7(\text{stat}) \pm 0.9(\text{syst}) \text{ ps}. \quad (21)$$

The combined result

$$\tau_\mu(\text{MuLan}) = 2\,196\,980.3 \pm 2.1(\text{stat}) \pm 0.7(\text{syst}) \text{ ps} \quad (22)$$

is obtained from the weighted average of the individual R06/R07 values with the appropriate accounting for the correlated uncertainties. The result corresponds to an overall uncertainty in the muon lifetime of 2.2 ps or 1.0 ppm.

Figure 28 and Table V summarizes the measurements of the positive muon lifetime over the past forty years. They include the MuLan R06 and R07 results, the MuLan commissioning measurement (Chitwood) [14], the FAST commissioning measurement (Barczyk) [12], and the earlier work of Duclos *et al.* [43], Balandin *et al.* [11, 44], Giovanetti *et al.* [9] and Bardin *et al.* [10]. The final result from the combined R06 and R07 datasets is a factor of 10(15) improvement over the MuLan(FAST) commissioning measurements and a factor of 30-150 improvement over the earlier experiments.

TABLE V: Compilation of post-1970 measurements of the positive muon lifetime. The first three entries are our final results from the combined R06+R07 datasets and the individual R06/R07 datasets. Barczyk *et al.* is the result of the FAST commissioning measurement and Chitwood *et al.* is the result of the MuLan commissioning measurement. The remaining entries are previous generations of lifetime experiments. In column one the uncertainty represents the combined statistical and systematic errors.

Measured lifetime ( $\mu\text{s}$ )	Reference	Publication year
$2.196\,9803 \pm 0.000\,0022$	R06+R07	
$2.196\,9799 \pm 0.000\,0027$	R06	
$2.196\,9812 \pm 0.000\,0038$	R07	
$2.197\,083 \pm 0.000\,035$	Barczyk [12]	2008
$2.197\,013 \pm 0.000\,024$	Chitwood [14]	2007
$2.197\,078 \pm 0.000\,073$	Bardin [10]	1984
$2.196\,95 \pm 0.000\,06$	Giovanetti [9]	1984
$2.197\,11 \pm 0.000\,08$	Balandin [11, 44]	1974
$2.197\,3 \pm 0.000\,3$	Duclos [43]	1973

The final result for  $\tau_\mu$  is in reasonable agreement with the earlier work of Duclos *et al.*, Balandin *et al.*, Giovanetti *et al.* and Bardin *et al.* While it is in reasonable agreement with the MuLan commissioning measurement (a difference of  $1.3\sigma$ ) it is in marginal disagreement with the FAST commissioning measurement (a difference of

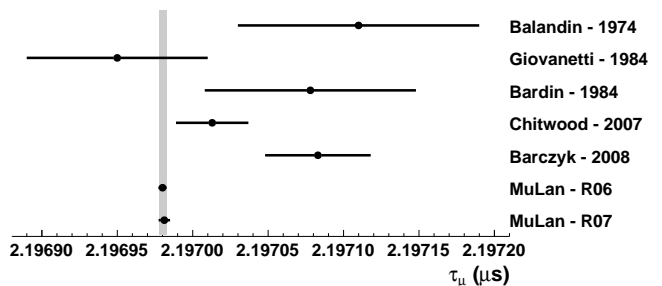


FIG. 28: Plot of post-1970 measurements of the positive muon lifetime. The data points represent the individual measurements and the vertical band corresponds to the combined R06 and R07 result. The result of Duclos *et al.* is not shown in the figure.

$2.9\sigma$ ). The weighted average of all results in Table V gives a lifetime  $\tau_\mu = 2\,196\,981.1 \pm 2.2$  ps with a chi-squared  $\chi^2/\text{dof} = 2.7$ . The weighted average is dominated by our final R06+R07 result with the poor chi-squared originating from the disagreement between our final result and the FAST commissioning result.

### C. Result for Fermi constant, $G_F$

We use the relation obtained by van Ritbergen and Stuart (vRS) [2–4] for the extraction of the Fermi constant  $G_F$  from a measurement of the muon lifetime  $\tau_\mu$ . The vRS relation is derived using the  $V$ - $A$  current-current Fermi interaction with QED corrections evaluated to 2-loop order. It yields

$$G_F = \sqrt{\frac{192\pi^3}{\tau_\mu m_\mu^5} \frac{1}{1 + \Delta q^{(0)} + \Delta q^{(1)} + \Delta q^{(2)}}} \quad (23)$$

where  $\tau_\mu$  is the measured muon lifetime,  $m_\mu$  is the measured muon mass, and  $\Delta q^{(0)}$ ,  $\Delta q^{(1)}$  and  $\Delta q^{(2)}$  are theoretical corrections with  $\Delta q^{(0)}$  accounting for the effects of the non-zero electron mass on the  $\mu$ -decay phase space and  $\Delta q^{(1/2)}$  accounting for the contributions of the 1-/2-loop radiative corrections to the  $\mu$ -decay amplitude. The effects of non-zero neutrino mass are completely negligible.

For the muon lifetime, the weighted average of the R06+R07 results,  $\tau_\mu = 2\,196\,980.3 \pm 2.2$  ps, is used. The determination of  $G_F$  in units of  $\text{GeV}^{-2}$  from the measurement of  $\tau_\mu$  in units of ps requires a unit conversion via Planck's constant,  $\hbar$ . For Planck's constant, the value recommended by the 2010 CODATA committee [6] of  $\hbar = 6.582\,119\,28(15) \times 10^{-25} \text{ GeV} \cdot \text{s}$  is used.

For the muon mass, the recommended value of  $m_\mu = 105.658\,371\,5(35) \text{ MeV}$  [6] is used. This value is derived from the combination of the measurements of the electron mass and the electron-to-muon mass ratio.

Computing the theoretical corrections requires both the electron-to-muon mass ratio  $m_e/m_\mu$  and the fine

structure constant  $\alpha(m_\mu)$  at the momentum transfer  $q = m_\mu$  of the  $\mu$ -decay process. The recommended value of  $m_e/m_\mu = 4.836\,331\,66(12) \times 10^{-3}$  [6] is used. For the fine structure constant  $\alpha(m_\mu)$  the value  $\alpha(m_\mu) = 1.0/135.902\,660\,087(44)$  is used. The value is obtained from Eqn. 4.13 of van Ritbergen and Stuart [2] using the CODATA value of the fine structure constant  $\alpha(0) = 1.0/137.035\,999\,074(44)$  [6] at zero-momentum transfer.

The value for the phase space term  $\Delta q^{(0)} = -187.1$  ppm is obtained from Eqn. 2.7 in Ref. [2] and the value for the 1-loop QED correction  $\Delta q^{(1)} = -4233.7$  ppm is obtained from Eqn. 2.8 in Ref. [2]. Note that Eqn. 2.8 of Ref. [2] incorporates the effects of the non-zero electron mass on the 1-loop QED correction.<sup>21</sup>

The value for the 2-loop QED correction  $\Delta q^{(2)} = +36.3$  ppm is obtained by summing the individual contributions from purely-photonic loops (Eqn. 9 in Ref. [3]), electron loops (Eqn. 10 in Ref. [3]), muon loops (Eqn. 19 in Ref. [4]), tau loops (Eqn. 20 in Ref. [4]) and hadronic loops (Eqn. 16 in Ref. [4]). Additionally, a correction of  $-0.4$  ppm, first evaluated by Pak and Czarnecki [5], is included to account for the effects of the non-zero electron mass on the 2-loop QED correction.

Using Eqn. 23 and the aforementioned values for the  $\tau_\mu$ ,  $m_\mu$ , and the theoretical corrections  $\Delta q^{(0)}$ ,  $\Delta q^{(1)}$  and  $\Delta q^{(2)}$ , we obtain

$$G_F(\text{MuLan}) = 1.166\,378\,7(6) \times 10^{-5} \text{ GeV}^{-2} \quad (0.5 \text{ ppm}). \quad (24)$$

This result represents a thirty-fold improvement over the 1999 PDG value obtained before the vRS theoretical work and the lifetime measurements pre-dating MuLan.

The error in  $G_F$  of 0.5 ppm is dominated by the 1.0 ppm uncertainty of the muon lifetime measurement with additional contributions of 0.08 ppm from the muon mass measurement and 0.14 ppm from the theoretical corrections in Eqn. 23. Note the theoretical uncertainty of 0.3 ppm originally quoted by van Ritbergen and Stuart [2–4] arose from estimates of electron mass terms in the 2-loop QED corrections (0.17 ppm), hadronic contributions in the 2-loop QED corrections (0.02 ppm), and 3-loop QED corrections (0.14 ppm). Subsequently, Pak and Czarnecki [5] extended the work of vRS and calculated the 2-loop order, electron mass terms. Consequently, the overwhelming theoretical uncertainty is now the 0.14 ppm contribution associated with 3-loop QED corrections. The uncertainties associated with  $\hbar$ ,  $m_e/m_\mu$  and  $\alpha(m_\mu)$  are all negligible.

The determination of  $G_F$  from  $\tau_\mu$  has additionally been discussed by Erler and Langacker in the PDG Reviews of Particle Physics [46]. Their articles first appeared in 1992 with later updates as measurements improved and

theory advanced. The authors maintained a formulation that differs slightly from vRS with their placement of the phase space correction  $F(\rho)$  as a multiplicative factor for the radiative corrections, *e.g.*

$$\frac{1}{\tau_\mu} = \frac{G_F^2 m_\mu^5}{192\pi^3} F(\rho) \left[ 1 + H_1(\rho) \frac{\alpha(m_\mu)}{\pi} + H_2(\rho) \frac{\alpha^2(m_\mu)}{\pi^2} \right] \quad (25)$$

where  $\rho = m_e^2/m_\mu^2$  is the electron-muon mass ratio squared,  $\alpha(m_\mu)$  is the fine structure constant evaluated at the relevant momentum transfer, and  $H_1(\rho)$  and  $H_2(\rho)$  represent the 1- and 2-loop radiative corrections. Although the phase space correction  $F(\rho)$  is identical to  $1 + \Delta q^{(0)}$ , and the 1-loop radiative correction  $F(\rho)H_1(\rho)\alpha(m_\mu)/\pi$  is identical to  $\Delta q^{(1)}$  (see Ref. [45]), the 2-loop radiative corrections  $F(\rho)H_2(\rho)\alpha^2(m_\mu)/\pi^2$  and  $\Delta q^{(2)}$  differ by  $F(\rho)$ —thus introducing a small inconsistency between Eqn. 23 of vRS and Eqn. 25 of Erler and Langacker. However, as  $F(\rho) = 0.99981295$  is almost unity, the evaluation of  $G_F$  using Eqn. 23 and Eqn. 25 gives the same value to a precision 0.1 ppm.<sup>22</sup>

The above extraction of  $G_F$  from  $\tau_\mu$  is based on the assumption of the  $V - A$  chiral structure of the charged-current interaction. If the assumption of the  $V - A$  character is relinquished, the relation between  $\tau_\mu$  and  $G_F$  is modified [47].

## D. Discussion of results

Below we compare the results from the AK-3 (R06) dataset and the quartz (R07) dataset and comment on the significance of the 1.0 ppm measurement of the muon lifetime and the 0.5 ppm determination of the Fermi constant.

### 1. Comparison between R06/R07 datasets

The two values of  $\tau_\mu$  extracted from the R06/R07 datasets are in good agreement. Because the two datasets involved different targets having greatly varying magnitudes, time dependencies and angular distributions of  $\mu\text{SR}$  signals, the natural interpretation is that the spin rotation aspects have been properly handled.

However, a second concern for a precision lifetime measurement is any difference between the positive muon lifetime in free space and the positive muon lifetime in matter. For example, a muon can reside in matter as either a bound muonium atom or an unbound positive muon. The relative populations of bound muonium and

<sup>21</sup> The 1-loop QED correction including electron mass effects was originally derived by Nir [45].

<sup>22</sup> In addition, the expressions used by vRS and Erler and Langacker to evaluate the running of  $\alpha(m_\mu)$  are slightly different. However, these differences are numerically unimportant for the Fermi constant at the part-per-million level.

unbound  $\mu^+$ 's can vary with material and ranges from small muonium fractions (*e.g.* AK-3) to large muonium fractions (*e.g.* quartz). A significant difference in lifetimes between muonium and  $\mu^+$ 's could jeopardize the interpretation of lifetime measurements using stopped muons.

We stress: the two targets involve different populations of  $\mu^+$ 's (the dominant species in AK-3) and muonium atoms (the dominant species in quartz). The possibility of a lifetime difference between the free muon and the muonium atom was addressed by Czarnecki, LePage and Marciano [48]. They found that the leading-order contributions from the two largest corrections—the  $\mu^+e^-$  binding energy and  $e^+e^-$  final-state interaction—cancel out and the resulting difference between their lifetimes to be only  $\sim 0.6$  parts-per-billion.<sup>23</sup> This difference is negligible compared to the part-per-million precision of the R06/R07 lifetime measurements.

In addition, a lifetime difference between free muons and muonium atoms could arise from  $\mu^+e^-$  annihilation in muonium atoms. For example, the rate of  $\mu^+e^- \rightarrow \bar{\nu}_\mu\nu_e$  annihilation was considered by Czarnecki *et al.* [48] and earlier by Li *et al.* [51]. However, the SM prediction for the annihilation rate is only  $10^{-13}$  of the muon decay rate and therefore negligible compared to the ppm precision of the R06/R07 lifetime measurements.

### 2. Relevance to precision muon capture studies

A precise determination of  $\tau_\mu$  is important to current work on nuclear muon capture. The MuCap experiment [52] has recently measured the  $\mu^-p$  singlet capture rate  $\Lambda_s$  and the MuSun experiment [53] is presently measuring the  $\mu^-d$  doublet capture rate  $\Lambda_d$ . Both experiments derive the muon capture rates from the tiny difference ( $\Lambda_o - \Lambda$ ) between the positive muon decay rate ( $\Lambda_o = 1/\tau_{\mu^+}$ ) and the muonic atom disappearance rates ( $\Lambda = 1/\tau_{\mu^-Z}$ ). Because the capture rates are very small, a precise determination of the muonic atom disappearance rates and the free muon decay rate is necessary.

Prior to this work the muon decay rate  $\Lambda_o$  was known to 9 ppm or  $5\text{ s}^{-1}$ , an uncertainty that limited the capture rate determinations from disappearance rate experiments. The new result for the muon lifetime—yielding a precision of 1 ppm or  $0.5\text{ s}^{-1}$  in  $\Lambda_o$ —has eliminated this source of uncertainty.

### 3. Relevance to fundamental constant determinations

In 1999 the uncertainty in  $G_F$  was 17 ppm, a combination of a 9 ppm experimental uncertainty and a 15 ppm theoretical uncertainty. The combined outcome of the

vRS calculations [2, 3] and the MuLan experiment is a thirty fold reduction in the total uncertainty in the Fermi constant—to a precision 0.5 ppm.

The electroweak sector of the standard model involves three parameters, the two gauge coupling constants  $g, g'$  and the Higgs energy density  $v$ . Their values are fixed by measurements of the fine structure constant,  $\alpha$ , Fermi coupling constant,  $G_F$ , and Z boson mass,  $M_Z$ . The thirty-fold improvement in the determination of  $G_F$ , together with recent improvements in the determinations of  $\alpha$  and  $M_Z$ , allows for improved tests of the Standard Model.

## VII. CONCLUSION

In summary, we report a measurement of the positive muon lifetime  $\tau_\mu$  to 1.0 ppm and a determination of the Fermi constant  $G_F$  to 0.5 ppm. The experiment used a novel, time-structured muon beam with a segmented, fast-timing, positron detector instrumented with 450 MHz waveform digitizer readout. The results for  $\tau_\mu$  and  $G_F$  are substantial improvements over earlier determinations from previous generations of lifetime experiments. Improved knowledge of  $\tau_\mu$  is important to other experimental programs and improved knowledge of  $G_F$  is important for numerous electroweak processes.

In the determination of the Fermi constant, we are fortunate that the uncertainties on many quantities—*e.g.* the muon mass and Planck's constant—are significantly below the ppm-level. To improve the determination of  $G_F$  by another order of magnitude will require, in addition to another order of magnitude improvement in  $\tau_\mu$ , a significant experimental improvement in the muon mass determination and a significant improvement in the various theoretical corrections.

## VIII. ACKNOWLEDGMENTS

We thank E. Morenzoni, R. Scheuermann and A. Stoykov for their assistance with  $\mu$ SR studies in AK-3 and quartz. We thank the PSI staff, especially D. Renker, K. Deiters, and M. Hildebrandt. We thank M. Barnes and G. Wait from TRIUMF for the development of the kicker, and thank N. Bondar, T. Ferguson and R. Prieels for their contributions to the electronics readout for the beam monitor. We also thank the National Center for Supercomputing Applications (NCSA) for supporting the data analysis, and the U.S. National Science Foundation for their financial support.

<sup>23</sup> This cancellation between final-state interaction effects and binding energy effects is familiar from work by Huff [49] and Uberall *et al.* [50] for muonic atoms. So-called Huff factors, that repre-

sent the difference between the  $\mu^-$  decay rate in free space and the  $\mu^-$  decay rate in muonic atoms, have been calculated across the periodic table. The calculated effects for bound negative muons are supported by experimental data from muonic atoms.

- [1] E. D. Commins and P. H. Bucksbaum, *Weak Interactions of Leptons and Quarks* (Cambridge University Press, Cambridge, UK, 1983).
- [2] T. van Ritbergen and R. G. Stuart, Nucl. Phys. **B564**, 343 (2000), arXiv:hep-ph/9904240 [hep-ph].
- [3] T. van Ritbergen and R. G. Stuart, Phys. Rev. Lett. **82**, 488 (1999), arXiv:hep-ph/9808283 [hep-ph].
- [4] T. van Ritbergen and R. G. Stuart, Phys. Lett. **B437**, 201 (1998), arXiv:hep-ph/9802341 [hep-ph].
- [5] A. Pak and A. Czarnecki, Phys. Rev. Lett. **100**, 241807 (2008), arXiv:0803.0960 [hep-ph].
- [6] P. J. Mohr, B. N. Taylor, and D. B. Newell, (2012), arXiv:1203.5425 [physics.atom-ph].
- [7] M. Awramik, M. Czakon, A. Freitas, and G. Weiglein, Phys. Rev. **D69**, 053006 (2004), arXiv:hep-ph/0311148 [hep-ph].
- [8] C. Caso *et al.* (Particle Data Group), Eur. Phys. J. **C3**, 1 (1998).
- [9] K. Giovanetti, W. Dey, M. Eckhause, R. Hart, R. Hartmann, *et al.*, Phys. Rev. **D29**, 343 (1984).
- [10] G. Bardin, J. Duclos, A. Magnon, J. Martino, E. Zavattini, *et al.*, Phys. Lett. **B137**, 135 (1984).
- [11] M. Balandin, V. Grebenyuk, V. Zinov, A. Konin, and A. Ponomarev, Sov. Phys. JETP **40**, 811 (1975).
- [12] A. Barczyk *et al.* (FAST Collaboration), Phys. Lett. **B663**, 172 (2008), arXiv:0707.3904 [hep-ex].
- [13] R. M. Carey *et al.*, PSI proposal R-99-07 (1999).
- [14] D. Chitwood *et al.* (MuLan Collaboration), Phys. Rev. Lett. **99**, 032001 (2007), arXiv:0704.1981 [hep-ex].
- [15] D. Webber *et al.* (MuLan Collaboration), Phys. Rev. Lett. **106**, 041803 (2011), arXiv:1010.0991 [hep-ex].
- [16] M. Barnes and G. Wait, IEEE Trans. Plasma Sci. **32**, 1932 (2004).
- [17] R. Armenta, M. Barnes, and G. Wait, in *Pulsed Power Conference, 2005 IEEE* (2005) pp. 676–679.
- [18] *Struck SIS3600 32-bit VME event latch*, Struck Innovative System, Harksheider Str. 102A, 22399 Hamburg, Germany (), <http://www.struck.de>.
- [19] *Arnokrome<sup>TM</sup> III: Bar, Rod, and Wire*, Arnold Engineering Company, Arnold Magnetic Technologies, 770 Linden Ave, Rochester, NY 14625 (2004), <http://www.arnoldmagnetics.com>.
- [20] J. F. Ziegler, Nucl. Instrum. Methods **B219-220**, 1027 (2004), proc. of the Sixteenth Int. Conf. on Ion Beam Analysis.
- [21] E. Morenzoni and H. Luetkins, private communication.
- [22] Boston Piezo-Optics Inc., 38 B Maple Street Bellingham, MA 02019 USA, <http://www.bostonpiezooptics.com>.
- [23] K. Halbach, Nucl. Instrum. Methods **187**, 109 (1981).
- [24] W. K. Dawson, K. Nishiyama, and K. Nagamine, Hyperfine Interactions **86**, 753 (1994), 10.1007/BF02068975.
- [25] J. H. Brewer, G. D. Morris, D. J. Arseneau, D. G. Eshchenko, V. G. Storchak, and J. Bermejo, Physica **B289-290**, 425 (2000).
- [26] Saint-Gobain Crystals, 17900 Great Lakes Pkwy, Hiram, OH 44234-9681 USA, <http://www.crystals.saint-gobain.com/>.
- [27] PHOTONIS USA, P.O. Box 1159, Sturbridge, MA 01566., <http://www.photonis.com>.
- [28] ADIT/Electron Tubes, 100 Forge Way, Unit F, Rockaway, NJ 07866, <http://www.electrontubes.com>.
- [29] Laser Photonics, Inc., 12351 Research Parkway, Orlando, Florida 32826., <http://www.laserphotonics.com/>.
- [30] *E4400B ESG-A Series Analog RF Signal Generator*, Agilent Technologies, 5301 Stevens Creek Blvd., Santa Clara, CA 95051, <http://www.agilent.com>.
- [31] V. Tishchenko, S. Battu, S. Cheekatmalla, D. Chitwood, S. Dhamija, T. Gorringer, F. Gray, K. Lynch, I. Logashenko, S. Rath, and D. Webber, Nucl. Instrum. Methods **A592**, 114 (2008).
- [32] E. Frlez, D. Pocanic, K. A. Assamagan, Y. Bagaturia, V. A. Baranov, W. Bertl, C. Brnnimann, M. Bychkov, J. F. Crawford, M. Daum, T. Flgel, R. Frosch, R. Horisberger, V. A. Kalinnikov, V. V. Karpukhin, N. V. Khomutov, J. E. Koglin, A. S. Korenchenko, S. M. Korenchenko, T. Kozlowski, B. Krause, N. P. Kravchuk, N. A. Kuchinsky, W. Li, D. W. Lawrence, R. C. Minehart, D. Mzhavia, H. Obermeier, D. Renker, B. G. Ritchie, S. Ritt, T. Sakhelashvili, R. Schnyder, V. V. Sidorkin, P. L. Slocum, L. C. Smith, N. Soic, W. A. Stephens, I. Supek, Z. Tsamalaidze, B. A. VanDevennder, Y. Wang, H. P. Wirtz, and K. O. H. Ziock, Nucl. Instrum. Methods **A526**, 300 (2004).
- [33] R. Brun and F. Rademakers, Nucl. Instrum. Methods **A389**, 81 (1997).
- [34] *Struck SIS3100/1100 PCI-to-VME interface*, Struck Innovative System, Harksheider Str. 102A, 22399 Hamburg, Germany (), <http://www.struck.de>.
- [35] D. Huffman, Proceedings of the IRE **40**, 1098 (1952).
- [36] P. Deutsch, “GZIP file format specification version 4.3,” RFC 1952 (Informational) (1996).
- [37] P. Deutsch and J.-L. Gailly, “ZLIB Compressed Data Format Specification version 3.3,” RFC 1950 (Informational) (1996).
- [38] National Center for Supercomputing Applications, 1205 W. Clark St., Room 1008, Urbana, IL 61801, <http://www.ncsa.uiuc.edu>.
- [39] G. Bennett *et al.* (Muon G-2 Collaboration), Phys. Rev. **D73**, 072003 (2006), arXiv:hep-ex/0602035 [hep-ex].
- [40] W. H. Press, S. A. Teukolsky, W. T. Vetterling, and B. P. Flannery, *Numerical Recipes: The Art of Scientific Computing*, 3rd ed. (Cambridge University Press, 2007).
- [41] F. James and M. Roos, Comput. Phys. Commun. **10**, 343 (1975).
- [42] R. Scheuermann and A. Stoykov, private communication.
- [43] J. Duclos, A. Magnon, and J. Picard, Phys. Lett. **B47**, 491 (1973).
- [44] M. Balandin, V. Grebenyuk, V. Zinov, A. Konin, and A. Ponomarev, Zh. Eksp. Teor. Fiz. [Sov. Phys. – JETP] (1974).
- [45] Y. Nir, Phys. Lett. **B221**, 184 (1989).
- [46] J. Beringer *et al.* (Particle Data Group), Phys. Rev. **D86**, 010001 (2012).
- [47] N. Danneberg, W. Fetscher, K.-U. Köhler, J. Lang, T. Schweizer, A. von Allmen, K. Bodek, L. Jarczyk, S. Kistryn, J. Smyrski, A. Strzałkowski, J. Zejma, K. Kirch, A. Kozela, and E. Stephan, Phys. Rev. Lett. **94**, 021802 (2005).
- [48] A. Czarnecki, G. Lepage, and W. J. Marciano, Phys. Rev. **D61**, 073001 (2000), arXiv:hep-ph/9908439 [hep-ph].
- [49] R. W. Huff, Ann. Phys. (N. Y.) **16**, 288 (1961).

[50] H. Überall, Phys. Rev. **119**, 365 (1960).

[51] P.-J. Li, Z.-Q. Tan, and C.-E. Wu, J. Phys. G **14**, 525 (1988).

[52] V. Andreev *et al.* (MuCap Collaboration), Phys. Rev. Lett. **99**, 032002 (2007), arXiv:0704.2072 [nucl-ex].

[53] V. Andreev *et al.* (MuSun Collaboration), (2010), arXiv:1004.1754 [nucl-ex].